Journal of Microwaves, Optoelectronics and Electromagnetic Applications, Vol. 21, No. 4, December 2022
DOI: http://dx.doi.org/10.1590/2179-10742022v21i4263644

Simulation of Current Pulses and Sound Waves Resulting from Partial Discharges in a Needle-Plane Geometry in Air

Luís Victor Muller Fabris, Jean Carlos Cardozo da Silva
Graduate Program in Electric and Computer Engineering, Universidade Tecnológica Federal do Paraná, Curitiba, Paraná, Brazil, luis.victor.m@gmail.com, jeanccs@utfpr.edu.br

***Abstract*— Partial discharges can occur in different types of electric equipment and cause progressive insulation deterioration, so there is interest in monitoring partial discharges for assessing the state of the isolation of an electric system and to predict failures. Techniques to detect partial discharges, such as detecting ultrasonic emission, have been proposed in the literature, but as various effects can co-occur during a discharge, identifying characteristics in sound and pressure waveforms and correlating then with discharge characteristics is difficult. Simulations can assist in these correlations by allowing the isolation of the different phenomena. In this work the drift diffusion model, including photoionization, is coupled with the linearized compressible Navier-Stokes equations to simulate ultrasonic waves produced by partial discharges. Previous works have used the incompressible Navier-Stokes equations, so they can simulate ionic wind produced by the Trichel pulses, but no sound. In the literature, simulations have focused either on streamers or Trichel pulses. In this work both discharges and produced sound waves are successfully simulated for the needle-plane geometry in air. The electric current and charge per pulse are compared with experimental results reported in the literature for the same discharge conditions. The simulations have demonstrated that the sound waves depart from the electrode tip for the Trichel pulses, and for the streamers two sound waves are produced, one from the electrode tip and the other from the whole discharge length. Differences in the wave front with respect to the relative position to the electrode tip were analyzed, showing that near the discharge spot the sound wave is not a spherical wavefront. The sound wave for one of the discharges in the Trichel pulse regime was compared with experimental results in the literature. Results are in good agreement with the experimental data found in the literature. Both current and sound waves were successfully predicted and correlated with the discharge, results that can be used to help in the detection of partial discharges.**

***Index Terms*—** Partial discharges, Trichel Pulses, Streamers, drift-diffusion, Sound waves, Navier-Stokes.

I. INTRODUCTION

A Partial Discharge (PD) is a localized dielectric breakdown that does not completely bridge the insulation between two conductors. PDs can occur in different types of electric equipment that operate with high voltage, like generators, transformers and transmission lines. PDs are external when they occur from a conductor or insulation to the atmospheric air, but they can also be internal [1].

Brazilian Microwave and Optoelectronics Society-SBMO *received 02 May 2022; for review 12 May 2022; accepted 25 Sept 2022*
Brazilian Society of Electromagnetism-SBMag *ISSN 2179-1074*

On electric cables the internal PDs occur on voids inside the insulation that are filled with gas. These voids can be created during the fabrication process of the electric cable, or due to degradation after installation [2]. Degradation after installation occurs due to factors like exposure to solar radiation, humidity or mechanical factors such as bends or vibration [3], [4].

Partial discharges can produce ozone, which can cause erosion of polymeric insulation, and nitrogen oxides, which cause corrosion in metals when combined with water. Once initiated, a PD causes progressive deterioration of the insulation, leading to full dielectric breakdown. Monitoring partial discharges makes it possible to discover flaws in the insulation and quantify the gravity of these flaws before a complete failure; therefore, there is a great interest in detecting the PDs to assess the state of the isolation of a system [5]–[8].

Many different phenomena can be used to detect PDs such as fast current pulses with a rise time of few nanoseconds, sound waves on ultrasound frequencies, electromagnetic emission in the radio, UHF and visible light frequencies, heating and chemical reactions. Various methods have been used to detect PDs by measuring these phenomena, e.g., it is possible to detect the current pulses using coupling capacitors connected to a machine terminal or high frequency current transformers mounted on electric cables. It is also possible to detect the PDs using ultrasound sensors, UHF detectors, by monitoring temperature or by analyzing chemical substances produced by the electric discharges [6], [8]–[11].

Another possibility is to use Fiber Bragg Gratings to measure the ultrasonic emission of PDs [12], [13] or distributed optical fiber vibration sensors [14]. Fiber optic based sensors are insensitive to electromagnetic interference and, due to their small size, have fast response time to ultrasonic signals, which are ideal characteristics for measurement of PDs in underground transmission lines. Additionally, multiplexed Fiber Bragg Gratings distributed along an optical fiber could be buried parallel to the electric cable providing multiple measurement points.

Partial discharges have unique current and sound signatures. These signatures can help differentiate a PD from other noise sources and provide information about the PD intensity.

Various effects co-occur during a partial discharge, contributing to current and sound pressure, so identifying characteristics in current and sound waveforms and correlating them with discharge characteristics is difficult. In this sense, the study of models and methods for the accurate simulation of PDs and the resulting sound waves can help with this task and are of great interest.

Previous works reported in the literature have simulated partial discharges but have focused mainly on the electric current characteristics. Two main models have been used; the first, which is only valid for cavities in dielectrics, models the discharge as an instantaneous process that occurs when the electric field passes a critical value [1], [7], [15]. This model does not consider the discharge current pulse characteristics such as rise time and fall time, so it is not appropriate for simulating produced sound waves. The second, models the discharge process by solving three coupled drift-diffusion equations, which calculate the time dependent concentration of electrons, positive and negative ions in the discharge gap [16]–[28]. This model can provide the discharge pulse characteristics and has been coupled with the incompressible Navier-Stokes for simulating the ionic wind generated by a corona discharge [24].

In this article the three species drift-diffusion model including photoionization model is coupled with the linearized compressible Navier-Stokes equations, which are appropriate for modeling both the sound waves and ionic wind. In previous works, the effects of background radiation are not accounted for; an

received 02 May 2022; for review 12 May 2022; accepted 25 Sept 2022

ISSN 2179-1074

artificial initial condition of a gaussian spot near the tip of the electrode of electrons and ions is used for initiating the discharge. In this paper the gaussian spot is not used, the initial concentration of all species is zero and the electric discharge is initiated from the background radiation term incorporated in the model. Also, differently from other works which focus either on streamers or corona discharge, both types of discharges are simulated using the same set of parameters.

The main goal of the simulations reported in this work is to assess the frequency and amplitude of ultrasonic waves and electric current pulses of different types of partial discharges. The simulations results are compared with experimental results found in the literature for discharge current and produced sound pressure over time.

II. THEORY

PDs can be classified into different types of electric discharges depending on the electric field intensity and distribution on the discharge location. Partial discharges start from initial free electrons and ions produced by ionization from background radiation, generated from cosmic rays or radioactive elements on the earth's surface. These electrons and ions drift between the discharge electrodes accelerated by the electric field, generating a small electric current. This current is initially limited by the number of available ions and electrons produced by the background radiation. If the electric field is high enough (above $120\ Td$ in air, or $3 \cdot 10^6\ V/m$ at atmospheric pressure) these free electrons ionize atoms producing more free electrons, as well as positive ions, at a higher rate than electrons and ions are lost to attachment, a process called electron avalanche [16]. This mechanism produces a higher concentration of charged species, causing an increase in the electric field and in the electric discharge current, and sustains the discharge even in the absence of background radiation. In this case the discharge is called self sustained.

In atmospheric air, the main molecules involved on this ionization process (1) are N_2 and O_2 [17]. The ionization process occurs where the electric field is stronger. In the needle plane configuration studied in this article, this process occurs mainly near the needle electrode tip or in regions with high charge concentration.

Fig. 1 summarizes the main reactions occurring during the electric discharge for the needle-plane geometry studied in this work.

$$e + N_2(O_2) \rightarrow 2e + N_2^+(O_2^+) \tag{1}$$

Electrons can attach to molecules, producing negative ions, as indicated by (2).

$$e + O_2 \rightarrow O_2^- \tag{2}$$

Alternatively, electrons can also recombine with positive ions (3), and negative ions can recombine with positive ions (4), generating neutral molecules.

$$e + O_2^+(N_2^+) \rightarrow O_2(N_2) \tag{3}$$

$$O_2^- + N_2^+ \rightarrow O_2 + N_2 \tag{4}$$

If the electrode from where the discharge occurs is on a negative potential with respect to the ground, positive ions that collide with the electrode cause secondary electron emission (SEE) into the

Brazilian Microwave and Optoelectronics Society-SBMO *received 02 May 2022; for review 12 May 2022; accepted 25 Sept 2022*
Brazilian Society of Electromagnetism-SBMag *ISSN 2179-1074*

discharge domain. In this situation, negative ions and electrons drift to the ground electrode, where the electron outflow occurs. If the electrode is in a positive potential with respect to the ground, electrons and negative ions are attracted towards the electrode (electron Outflow), and positive ions drift in the direction of the ground electrode.

During the discharge, photons in the wavelength range from $98\ nm$ to $102.5\ nm$ can be produced by de-excitation of N_2 molecules [18], which were excited by electron impact (5).

$$\begin{aligned} e + N_2 &\rightarrow e + N_2^* \\ N_2^* &\rightarrow N_2 + photon[98 - 102.5\ nm] \end{aligned} \tag{5}$$

These photons have energy to ionize oxygen molecules as in (6).

$$O_2 + photon[98 - 102.5\ nm] \rightarrow e + O_2^+ \tag{6}$$

These photons have little effect on negative corona discharge since, in this case, the secondary electron emission produces significantly more electrons but plays a vital role in maintaining the positive corona discharge. These photons are also fundamental in explaining the propagation of positive streamers.

During a partial discharge, the charged species concentration is high enough to be considered as a fluid, so the time dependent concentration of each species can be modeled by the continuity equation (7), where c is the fluid concentration and R is the generation and consumption term, which accounts for the reactions described above.

$$\frac{\partial c}{\partial t} + \vec{\nabla} \cdot \vec{j} = R \tag{7}$$

During the discharge, the charged species are constantly gaining momentum from the electric field and transferring momentum or causing reactions through collisions, partially losing this momentum in the process. If this process happens on a smaller time scale than the discharge effects being simulated, the fluid flux $\vec{j}$ can be replaced by the sum of the diffusive flux $-D\vec{\nabla}c$ and the convective flux expressed by the mean drift velocity in the field $\pm c\mu\vec{E}$, where μ is the charged species mobility.

Additionally the ionization reaction term $S_{ph}(\vec{r})$, which describes the ionization rate at point $\vec{r}$ by photons produced during the discharge, as described in (5) and (6) can be modeled using (8) [29]. $I(\vec{r}')$ is the photon emission rate at point $\vec{r}'$, and $g(|\vec{r} - \vec{r}'|)$ is the photon absorption function at distance $|\vec{r} - \vec{r}'|$ from the source.

$$S_{ph}(\vec{r}) = \int\int\int_{R^3} \frac{I(\vec{r}')g(|\vec{r} - \vec{r}'|)}{4\pi(|\vec{r} - \vec{r}'|)^2} dV' \tag{8}$$

The photon absorption function can be approximated as (9), where A_j, λ_j are the adjust constants, and p_{O_2} is the partial pressure of oxygen in air.

$$g(|\vec{r} - \vec{r}'|) \simeq p_{O_2}^2 |\vec{r} - \vec{r}'| \sum_{j=1}^{j=3} A_j e^{-\lambda_j p_{O_2} |\vec{r} - \vec{r}'|} \tag{9}$$

Using (8) is computationally very demanding since the integral must be computed over the entire simulation domain for every point $\vec{r}$ in the domain in each time step.

received 02 May 2022; for review 12 May 2022; accepted 25 Sept 2022

ISSN 2179-1074

DOI: http://dx.doi.org/10.1590/2179-10742022v21i4263644

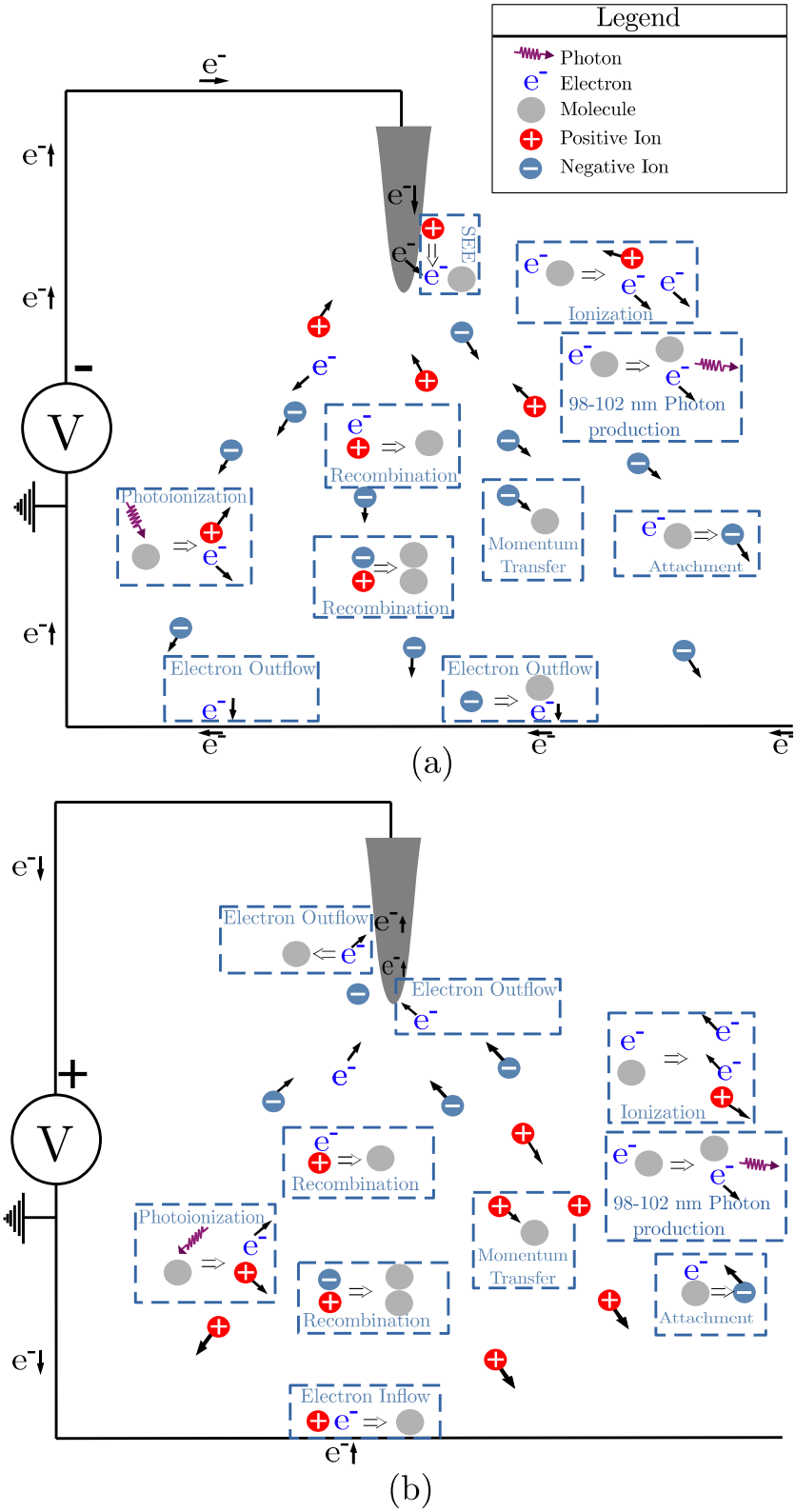

Fig. 1. Main reactions during electric discharge in a needle-plane geometry for: (a) the needle electrode in negative potential with respect to the plane electrode (ground); (b) the needle electrode in positive potential with respect to the plane electrode (ground).

Brazilian Microwave and Optoelectronics Society-SBMO *received 02 May 2022; for review 12 May 2022; accepted 25 Sept 2022*
Brazilian Society of Electromagnetism-SBMag

ISSN 2179-1074

It can be demonstrated analytically by solving using Green's function and Fourier transform that (8) is the solution to the sum of screened Poisson equations (10). Solving the three screened Poisson equations (10) is much less computationally demanding than solving (8) and gives the same solution.

$$\begin{gathered}\left[\nabla^2-(\lambda_j p_{o_2})^2\right] S_{ph}^j(\vec{r})=-A_j(p_{o_2})^2 I(\vec{r}) \\ S_{ph}(\vec{r})=\sum_{j=1}^{3} S_{ph}^j(\vec{r})\end{gathered} \tag{10}$$

The type of electric discharge depends on the electric field amplitude. For the lower electric field amplitudes, the corona discharge in the Trichel pulse regime occurs, as shown in Fig. 2. This electric discharge is characterized by a uniform glow around the electrode, where the electric field is stronger and ionization occurs, produced by electron-ion attachment. In positive corona discharge, positive ions drift away from the electrode. In negative corona discharge negative ion clouds drift away from the electrode, the Trichel Pulses [16]–[18]. In both discharges the current is composed of high frequency pulses, with a rise time in the order of nanoseconds, separated by microseconds [18], [30]. When the electric field is larger, the ion clouds merge, generating a stable discharge. In atmospheric air the fast transition to streamers occurs [18].

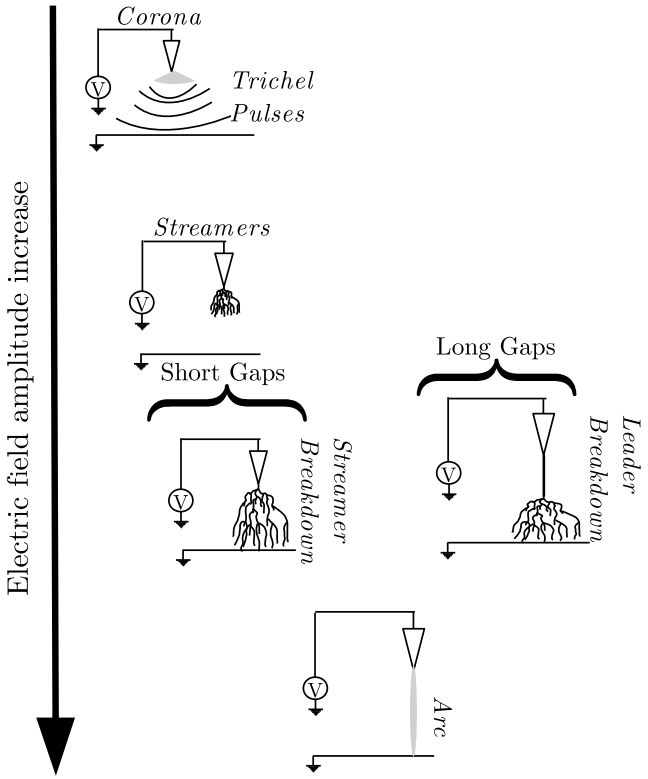

Fig. 2. Electric discharges as a function of the electric field intensity.

Streamers occur when the charge concentration distorts the electric field significantly. In this case, a region with a high ionization rate is formed, the streamer tip. In the case of negative streamers, electrons generated in this region drift to the front, generating more ions and causing the tip to move away from the negative electrode. In the case of positive streamers, the electrons are generated in front of the streamer tip by ionization from photons produced in the tip. These electrons generate positive

  ISSN 2179-1074

ions in front of the tip by ionization, causing the tip to move away from the positive electrode. In either case, the streamer can be described as an "ionization wave" [31].

One streamer tip can divide because of the stochastic charge distribution generated by background radiation, generating multiple streamer channels [16], [19], [31].

On long gaps, a single channel called leader forms from the union of multiple streamer channels, from where the streamers emerge. The leader is a channel with a higher temperature and ionization rate. If the streamers reach the ground electrode, a full gap breakdown can occur, with the transition to an electric arc [16]. The electric arc is a discharge sustained from thermionic electron emission from the electrode, differently from the previous ones. Because of this, the current carried by the arc is much higher than the previous discharges, and the arc can not be considered a partial discharge [16].

III. METHODS

Electric discharge simulations were carried out by solving three continuity equations (7), one for each charged fluid (electrons, positive and negative ions) being considered, so the concentration of electrons n_e, positive ions n_p, and negative ions n_n, are obtained by solving (11), (12), (13). These are the equations for the three species drift-diffusion model, which is solved using the Finite Element method. These equations account for the drift of the charged species under the electric field, diffusion, ionization (1), attachment (2), and recombination (3) and (4) reactions. The photon emission rate $I(\vec{r})$, described in (5), is calculated by (14), and the photo-ionization rate $S_{ph}(\vec{r})$, described in (6), is obtained using the three screened Poisson equations (15) and (16) as described in (10), (9) and (8). Functions μ_e, μ_p and μ_n are respectively the mobility of an electron, a positive ion, and a negative ion, whereas D_e, D_p and D_n are respectively the diffusion coefficient of an electron, a positive ion, and a negative ion. The function α is the coefficient of ionization of neutral molecules (1), η is the attachment coefficient of electrons and neutral molecules (2), k_{ep} is the coefficient of recombination of electrons and positive ions (3) and k_{np} is the coefficient of recombination of negative and positive ions (4). The vacuum permittivity is ϵ_0, and e is the modulus of electron charge. All of these coefficients are presented in Table I.

$$\frac{\partial n_e}{\partial t} - \vec{\nabla}\cdot(\mu_e n_e \vec{E} + D_e \vec{\nabla} n_e) = S_{ph} + \frac{n_e|\mu_e \vec{E}|}{(\alpha-\eta)^{-1}} - k_{ep} n_e n_p + S_b \tag{11}$$

$$\frac{\partial n_p}{\partial t} + \vec{\nabla}\cdot(\mu_p n_p \vec{E} - D_p \vec{\nabla} n_p) = S_{ph} + \alpha n_e|\mu_e \vec{E}| - k_{ep} n_e n_p - k_{np} n_n n_p + S_b \tag{12}$$

$$\frac{\partial n_n}{\partial t} + \vec{\nabla}\cdot(-\mu_n n_n \vec{E} - D_n \vec{\nabla} n_n) = \eta n_e|\mu_e \vec{E}| - k_{np} n_n n_p \tag{13}$$

$$I(\vec{r}) = \xi \frac{p_q}{p+p_q} \alpha \mu_e |\vec{E}| n_e \tag{14}$$

$$S_{ph}(\vec{r}) = \sum_{j=1}^{3} S_{ph}^{j}(\vec{r}) \tag{15}$$

$$\left[\nabla^2 - (\lambda_j p_{o_2})^2\right] S_{ph}^{j}(\vec{r}) = -A_j (p_{o_2})^2 I(\vec{r}); \quad \forall\ j \in \{1,2,3\} \tag{16}$$

Additionally, the Poisson equation (17) is used to calculate the electric potential V, and the electric

  ISSN 2179-1074

field, $\vec{E}$, is obtained from the relation $\vec{E} = -\vec{\nabla}V$. The effects of the magnetic field are neglected.

$$\nabla^2 V = \frac{|e|(n_e + n_n - n_p)}{\epsilon_0} \tag{17}$$

TABLE I. PARAMETERS USED IN THE SIMULATION

Coefficient	**Value**	**Coefficient**	**Value**
α	$2.135 \cdot 10^5 \exp(-1.3 \cdot 10^7/\lvert\vec{E}\rvert)\ m^{-1}$	S_b	$10^6\ m^{-3}s^{-1}$
η	$0.9 \cdot 10^3 \exp(-2.5 \cdot 10^6/\lvert\vec{E}\rvert)\ m^{-1}$	ρ_0	$1.2992\ Kg/m^3$
k_{ep}	$2 \cdot 10^{-13}\ m^3/s$	γ	0.0001
k_{np}	$2 \cdot 10^{-13}\ m^3/s$	D_e	$0.18\ m^2/s$
D_p	$0.028 \cdot 10^{-4}\ m^2/s$	μ_B	$1.8 \cdot 10^{-5} Pa \cdot s$
D_n	$0.043 \cdot 10^{-4}\ m^2/s$	β_s	$1/(\rho_0 \cdot v_0^2)$
μ_e	$1.9163 \cdot \lvert\vec{E}\rvert^{-0.25}\ m^2V^{-1}s^{-1}$	v_0	$340.6\ m/s$
μ_p	$2.43 \cdot 10^{-4}\ m^2V^{-1}s^{-1}$	Γ	1.4
μ	$1.82 \cdot 10^{-5}\ Pa \cdot s$	λ_3	$89.00\ Torr^{-1}m^{-1}$
p_{o_2}	$150\ Torr$	p_q	$60\ Torr$
p	$760\ Torr$	ξ	0.06
ϵ_0	$8.85 \cdot 10^{-12}\ C^2N^{-1}m^{-2}$	e	$1.602 \cdot 10^{-19}\ C$
A_1	$1.986\ m^{-2}Torr^{-2}$	A_2	$51\ m^{-2}Torr^{-2}$
A_3	$4886\ m^{-2}Torr^{-2}$	λ_1	$5.53\ Torr^{-1}m^{-1}$
λ_2	$14.60\ Torr^{-1}m^{-1}$	μ_n	$2.7 \cdot 10^{-4}\ m^2V^{-1}s^{-1}$

As the initial conditions it is assumed that $n_p(t=0) = n_e(t=0) = n_n(t=0) = 0$, so the discharge is initiated from background radiation term S_b, differently than other papers where the background radiation effect is ignored and the discharge is initiated from a gaussian spot placed at the electrode tip.

In this work, this model is used to simulate the corona discharge in Trichel pulse regime produced by an electrode on negative potential with respect to ground, as well as positive streamers.

From the electric field and electrons and ions concentrations obtained from the model (11), (12), (13), it is possible to obtain the electric discharge time dependent electric current i. Other works have utilized an approach described in [32], which contains approximations for simulations under constant electric field conditions.

In this paper, the equation for the discharge electric current without these approximations is derived from the Ampere Law, Gauss divergence theorem, and Poynting vector.

By taking the inner product of the Ampere law with the electric field $\vec{E}$ (18), expanding the left side using that $(\vec{\nabla} \times \vec{H}) \cdot \vec{E} = \vec{\nabla} \cdot (\vec{H} \times \vec{E}) + \vec{H} \cdot (\vec{\nabla} \times \vec{E})$, replacing the Poynting vector $\vec{S} = -\vec{H} \times \vec{E}$, and integrating in the discharge volume, (19) is obtained. The last term of (19) is zero as pointed since in the model the relation $\vec{E} = -\vec{\nabla}V$ is used, and $\vec{\nabla} \times \vec{E} = \vec{\nabla} \times (-\vec{\nabla}V) \equiv 0$.

$$(\vec{\nabla} \times \vec{H}) \cdot \vec{E} = \vec{J} \cdot \vec{E} + \epsilon_0 \frac{\partial \vec{E}}{\partial t} \cdot \vec{E} \tag{18}$$

$$-\int_V \vec{\nabla} \cdot \vec{S} dV = \int_V \vec{J} \cdot \vec{E} dV + \epsilon_0 \int_V \frac{\partial \vec{E}}{\partial t} \cdot \vec{E} dV - \int_V \vec{H} \cdot (\vec{\nabla} \times \vec{E}) dV \tag{19}$$

Applying the Gauss divergence theorem on the first term of (19), and noting that $-\int_S \vec{S} \cdot dA$ is equal

ISSN 2179-1074

to the electric power P supplied by the electrode, $P = V_{electrode}i$, (20) can be obtained.

$$i = \frac{1}{V_{eletrode}} \left[\int_V \vec{J} \cdot \vec{E} dV + \epsilon_0 \int_V \frac{\partial \vec{E}}{\partial t} \cdot \vec{E} dV \right] \tag{20}$$

In order to use (20), it is necessary to express the current density vector $\vec{J}$ in terms of the electrons and ions concentrations obtained from the model. The current density vector $\vec{J}$ can be obtained by replacing the charge density $\rho = |e|(n_p - n_e - n_n)$, which is obtained considering that the ions have charge $+e$ or $-e$, on the current continuity equation, as in (21).

$$\begin{gathered} -\vec{\nabla} \cdot \vec{J} = \frac{\partial \rho}{\partial t} = |e| \left(\frac{\partial n_p}{\partial t} - \frac{\partial n_e}{\partial t} - \frac{\partial n_n}{\partial t} \right) = \\ -|e|\vec{\nabla} \cdot (\mu_e n_e \vec{E} + D_e \vec{\nabla} n_e + \mu_p n_p \vec{E} - D_p \vec{\nabla} n_p + \mu_n n_n \vec{E} + D_n \vec{\nabla} n_n) + \\ +|e|(k_{np} n_n n_p - k_{ep} n_e n_p - k_{np} n_n n_p + k_{ep} n_e n_p - \eta n_e |\mu_e \vec{E}| + \eta n_e |\mu_e \vec{E}| + \\ +\alpha n_e |\mu_e \vec{E}| - \alpha n_e |\mu_e \vec{E}|) \end{gathered} \tag{21}$$

In this equation, the time derivatives of concentrations n_e, n_p and n_n are replaced with (11), (12) and (13).

Comparing the left and right terms in (21), (22) is obtained.

$$\vec{J} = |e|(\mu_e n_e \vec{E} + D_e \vec{\nabla} n_e + \mu_p n_p \vec{E} - D_p \vec{\nabla} n_p + \mu_n n_n \vec{E} + D_n \vec{\nabla} n_n) \tag{22}$$

The equation for the discharge electric current (23) based on parameters provided by the discharge simulation is obtained by replacing the obtained current density vector (22) in (20).

$$\begin{gathered} i = \frac{1}{V_{eletrode}} \left[|e| \int_V (\mu_e n_e \vec{E} + D_e \vec{\nabla} n_e + \mu_p n_p \vec{E} - D_p \vec{\nabla} n_p + \right. \\ \left. +\mu_n n_n \vec{E} + D_n \vec{\nabla} n_n) \cdot \vec{E} dV + \epsilon_0 \int_V \frac{\partial \vec{E}}{\partial t} \cdot \vec{E} dV \right] \end{gathered} \tag{23}$$

Replacing the numerically obtained results of (11), (12), (13), (14), (15), and (16), in (23), it is possible to obtain the discharge time dependent electric current i.

The propagation of the sound waves resulting from the electric discharge is simulated by using the linearized Navier-Stokes model, composed of the continuity equation (24), and the linearized Navier-Stokes momentum equation (25). In these equations, ρ_{air} is the perturbation in the air density associated with the sound waves, ρ_0 is the initial density of air, $\vec{u}$ is the velocity field of the sound wave, Γ is the ratio of specific heats, β_s is the isentropic compressibility, μ is the dynamic viscosity and μ_B is the bulk viscosity.

$$\frac{\partial \rho_{air}}{\partial t} + \vec{\nabla} \cdot (\rho_0 \vec{u}) = 0 \tag{24}$$

$$\rho_0 \left(\frac{\partial \vec{u}}{\partial t} \right) = \vec{F} - \vec{\nabla} \left(\frac{\rho_{air}}{\rho_0 \Gamma \beta_S} \right) + \mu(\nabla^2 \vec{u}) + (\mu_B + \frac{1}{3}\mu)\vec{\nabla}(\vec{\nabla} \cdot \vec{u}) \tag{25}$$

The sound wave is produced by a force per unity of volume generated due to the charged species in the presence of an electric field, modeled by $\vec{F}$ in the momentum equation (25), where $\vec{F} = |e|(n_p - n_e - n_n)\vec{E}$ [24]. This term links the discharge simulation using the drift-diffusion model to

received 02 May 2022; for review 12 May 2022; accepted 25 Sept 2022

ISSN 2179-1074

the linearized Navier-Stokes equations.

The pressure p_{sound} in function of time is obtained from the relation $p_{sound} = \rho_{air}/(\rho_0 \Gamma \beta_s)$. As the initial conditions for the Navier-Stokes equations it is assumed that $\vec{u}(t=0) = 0$ and $\rho(t=0) = 0$.

To prevent long simulations times, in this paper the simulations are carried for small time windows, which are enough to observe the behavior of the discharge pulse and produced sound wave. Normally transmission lines and other electrical equipments where PDs can occur work with alternating voltage in the 50 or 60 Hz range, but since the discharge charge concentration fluctuations occur very quickly, with changes that occur in less than one microsecond, the time varying applied voltage on the electrode do not affect the behavior of the discharge pulses in this small time window significantly. So, as a simplification, the simulations in this paper are carried under constant voltage.

All simulations were carried in the axisymmetric needle-plane geometry shown in Fig. 3. The electrode, which is in high voltage, is put at distance $d_{electrode}$ from the ground plate.

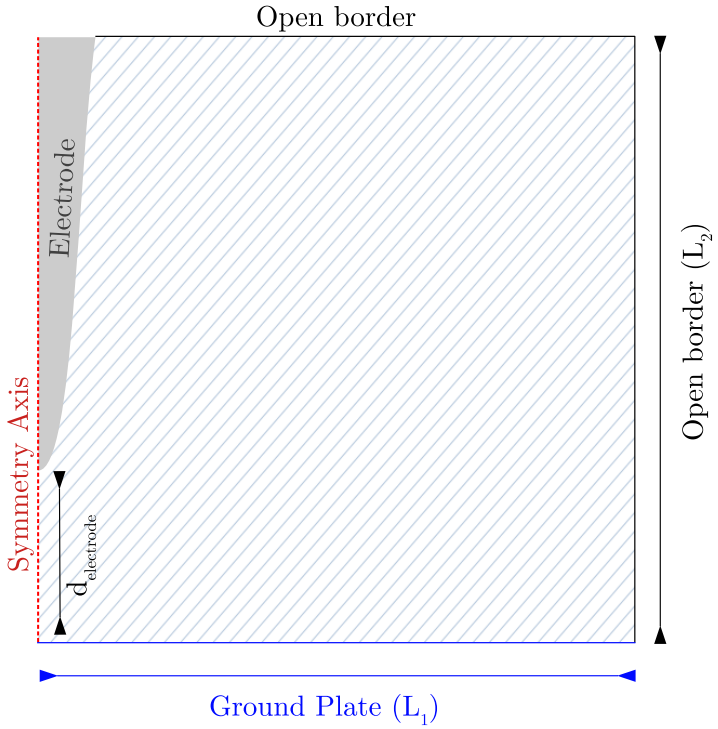

Fig. 3. The simulated 2D axisymmetric geometry. Calculations are carried on the hatched region.

The electrode format in the simulation is described by the parabola parametric equations (26) [33], where R is the electrode tip curvature radius.

$$\begin{aligned} r &= 2R \cdot t \\ z &= R \cdot t^2 + d_{electrode} \end{aligned} \tag{26}$$

The boundary conditions applied on the ground plate, electrode, and open border are listed in Table II for the discharge when the electrode is in negative potential with respect to the ground plate, and in Table III for the discharge when the electrode is on positive potential.

The boundary conditions on the open border are for infinity distance. The distances L_1 and L_2 shown in Fig. 3 need to be increased until the proximity to the discharge has no effect on the simulation. The

number of elements in the mesh increase with this distance, as well as the simulation RAM memory usage and run time, so this distance should not be too big to prevent the simulation from becoming unfeasible. The simulation also requires very thin elements near the electrode tip and where there are high ion concentrations during the discharge.

The mesh utilized has triangular elements, with sizes ranging from $0.3\ \mu m$ near the electrode tip, to $300\ \mu m$ far from the electrode tip. The total number of elements on the mesh varied from 717×10^3 to 3.5×10^6 depending on the electrode distance utilized, with the number of degrees of freedom varying from 2.8×10^6 to 9.8×10^6.

TABLE II. BOUNDARY CONDITIONS FOR NEGATIVE DISCHARGE

Electrode	**Ground plate**	**Open border**
$V = V_{electrode}$	$V = 0$	$\vec{E} \cdot \hat{n} = 0$
$n_n = 0$	$D_n(\hat{n} \cdot \vec{\nabla} n_n) = 0$	$n_n = 0$
$\vec{u} = 0$	$\vec{u} = 0$	$n_p = 0$
$\mu_e n_e \vec{E} + D_e \vec{\nabla} n_e = \gamma \eta_p \mu_p \lvert\vec{E}\rvert$	$D_e(\hat{n} \cdot \vec{\nabla} n_e) = 0$	$n_e = 0$
$D_p(\hat{n} \cdot \vec{\nabla} n_p) = 0$	$n_p = 0$	$\vec{u} = 0$
$S^i_{ph} = 0\ \forall\ i$	$S^i_{ph} = 0\ \forall\ i$	$S^i_{ph} = 0\ \forall\ i$

TABLE III. BOUNDARY CONDITIONS FOR POSITIVE DISCHARGE

Electrode	**Ground plate**	**Open border**
$V = V_{electrode}$	$V = 0$	$\vec{E} \cdot \hat{n} = 0$
$D_n(\hat{n} \cdot \vec{\nabla} n_n) = 0$	$D_p(\hat{n} \cdot \vec{\nabla} n_p) = 0$	$n_n = 0$
$\vec{u} = 0$	$\vec{u} = 0$	$n_p = 0$
$D_e(\hat{n} \cdot \vec{\nabla} n_e) = 0$	$n_n = 0$	$n_e = 0$
$n_p = 0$	$n_e = 0$	$\vec{u} = 0$
$S^i_{ph} = 0\ \forall\ i$	$S^i_{ph} = 0\ \forall\ i$	$S^i_{ph} = 0\ \forall\ i$

Simulations were carried out on Comsol Multiphysics® software using the PARDISO® solver. The Newton method was chosen with Jacobian update on every time step, 8 maximum iterations per time step, and a relative tolerance of 0.01. It is important for this simulation the use of a direct solver and Jacobian update on every time step to avoid convergence issues.

The Backward differentiation formula, which is normally used for problems involving convection and diffusion due to its stability, was used for the time stepping with minimal order of 1 and maximum order 2. Continuity equations were solved using streamline diffusion stabilization. All equations were solved using linear element order. The maximum RAM memory utilization varied from $18\ Gb$ to $55\ Gb$ depending on the number of degrees of freedom of the simulation, and simulation run time varied from 10 hours to 2.5 days on a Linux® computer with Intel Core® i9-10900 CPU @ 4GHz, 64 Gb RAM.

IV. RESULTS

Results of the simulation carried for $V_{electrode} = -6.5\ kV$ with an electrode-plane spacing of $6\ mm$ and electrode tip curvature radius of $35\ \mu m$ are shown in Figs. 4 to 8. In this simulation, the distances L_2 and L_1 for the open border, as shown in Fig. 3, were $46\ mm$ and $40\ mm$ respectively. Under these conditions, a discharge on the Trichel pulses regime is achieved, which is characterized by fast pulses of electric current separated by microseconds with fast rise times.

Fig. 4 shows the discharge current in the period from $31\ \mu s$ to $35\ \mu s$, which contains 3 Trichel pulses. This simulation produces a pulse period of $1.6\ \mu s$, with a charge per pulse of $73\ pC$ and an

received 02 May 2022; for review 12 May 2022; accepted 25 Sept 2022

ISSN 2179-1074

average current of 45 μA. Experimental results for this discharge can be obtained from [34], which uses the same needle-plane geometry, where the electrode used is a sewing needle connected to a DC high voltage negative power supply. In [34] the average DC current was measured with a dc microammeter, and the charge per pulse and pulse period were measured by analyzing the voltage drop, on a resistor in series with the discharge gap, with an oscilloscope. The oscilloscope was connected to the high voltage circuit through a blocking capacitor. The extrapolated experimental results from this article are a period of 1.67 μs, a charge per pulse of 65 pC, and an average current of 35 μA., which is in concordance with the simulation results.

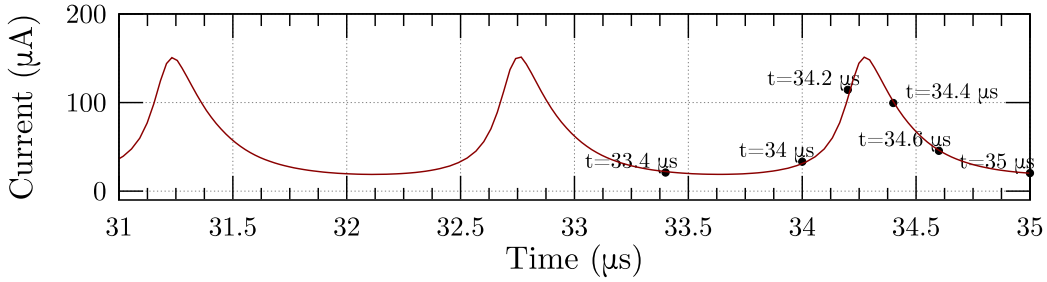

Fig. 4. Discharge current for $-6.5\ kV$, electrode-plane spacing of 6 mm and electrode tip curvature radius of 35 μm.

Figs. 5 and 6 show the surface concentration of ions and electrons as well as sound pressure taken for the specific times indicated in the third current pulse of Fig. 4. These results allow us to identify the different stages of the Trichel pulse formation. During the current pulse rise, which occurs from $t = 33.4\ \mu s$ to $t = 34.26\ \mu s$ the ionization occurring close to the electrode tip, due to the acceleration of electrons on the electric field and collisions with molecules, is causing the concentration of positive ions on a spot below the electrode tip to grow, which can be seen in the left column of Fig. 5 at times $t = 33.4\ \mu s$, $t = 34\ \mu s$ and $t = 34.2\ \mu s$.

The ionization and the secondary electron emission (SEE) process, due to the collision of positive ions with the electrode, generates more free electrons. The presence of this high concentration of positive ions near the electrode tip increases the electric field, which together with the availability of these free electrons increases the ionization rate, a process which is responsible for the fast growth of the current pulse.

Electrons created by the ionization eventually drift away from the positive ion spot, and generate negative ions by attachment which concentrate in a region just below the positive ion spot. This increase in the concentration of electrons and negative ions can be seen in the right column of Fig. 5 and the right column of Fig. 6, respectively [35]. Notice on the left column of Fig. 5 that during the pulse rise, the positive ion spot near the electrode tip is getting narrower. The high concentration of negative ions being formed ultimately causes a decrease in the electric field, which together with the narrowing of the positive ion spot, decreases the ionization rate significantly. This causes the concentrations, and the electric current to stop rising at $t = 34.26\ \mu s$.

After that, the electrons emitted from the SEE recombine with the positive ions, causing the concentration to reduce. The negative ion cloud slowly drifts away from the electrode, and the positive ion cloud size increases. After some time, when the negative ion cloud is far enough, the positive ion, electron concentrations and electric field reach a condition similar to the one they were at the beginning of the pulse, then another pulse occurs.

DOI: http://dx.doi.org/10.1590/2179-10742022v21i4263644

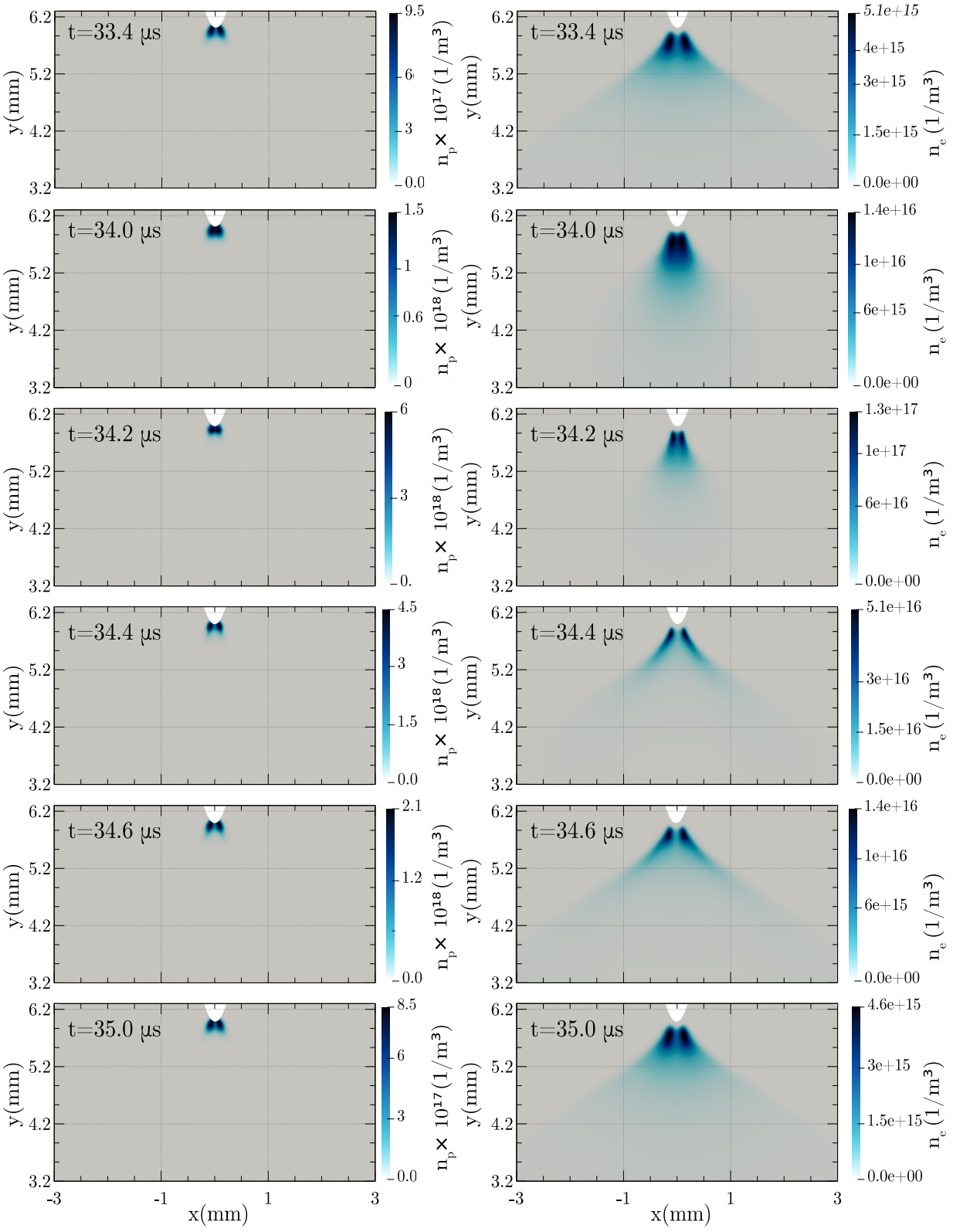

Fig. 5. Positive ion concentration (n_p) and electron concentration (n_e) for different times of the $-6.5\ kV$ discharge, electrode-plane spacing was $6\ mm$ and electrode tip curvature radius was $35\ \mu m$.

Brazilian Microwave and Optoelectronics Society-SBMO *received 02 May 2022; for review 12 May 2022; accepted 25 Sept 2022*
Brazilian Society of Electromagnetism-SBMag

ISSN 2179-1074

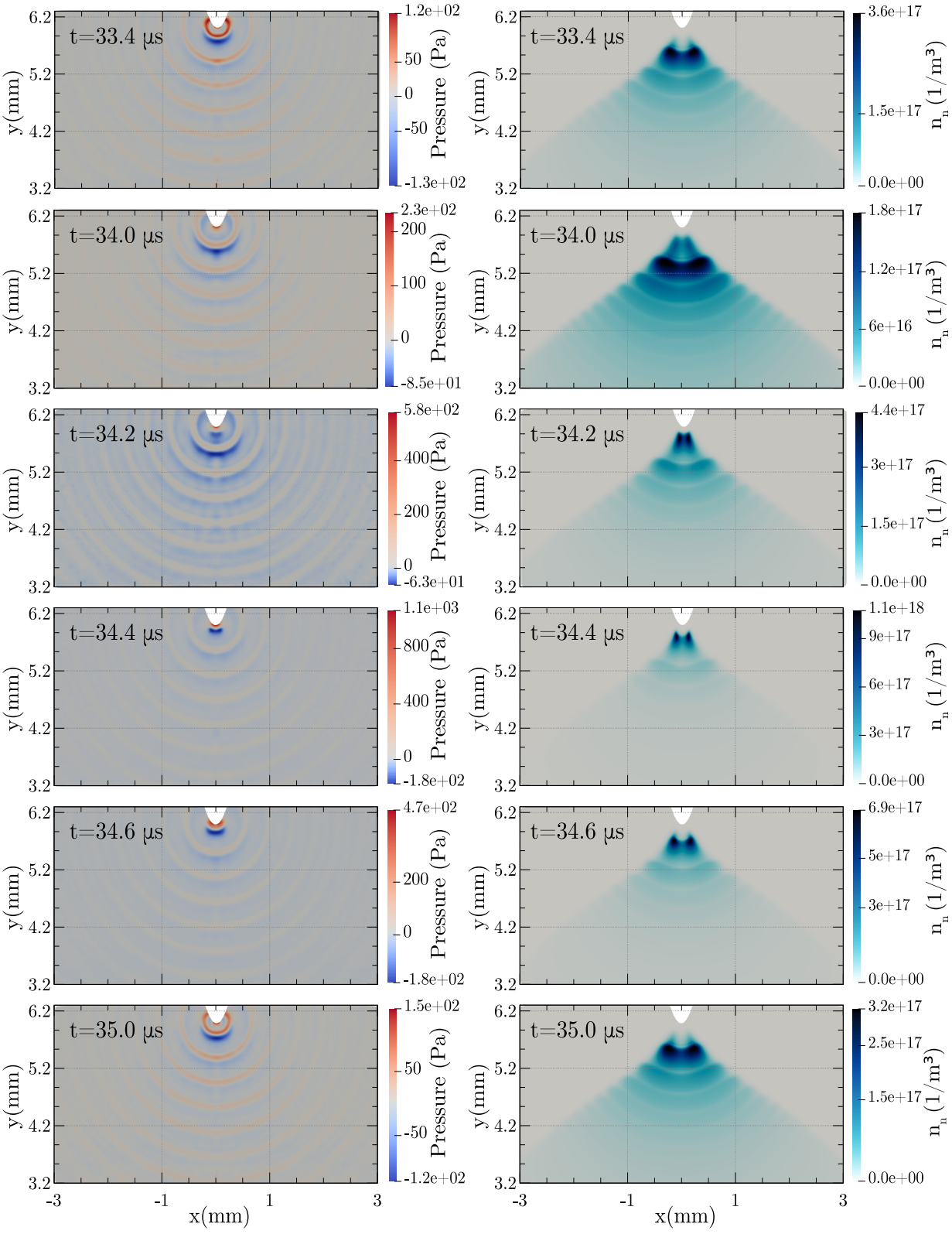

Fig. 6. Sound pressure and negative ion concentration (n_n) for different times of the $-6.5\ kV$ discharge with electrode-plane spacing of 6 mm and electrode tip curvature radius of 35 μm.

Brazilian Microwave and Optoelectronics Society-SBMO *received 02 May 2022; for review 12 May 2022; accepted 25 Sept 2022*
Brazilian Society of Electromagnetism-SBMag

ISSN 2179-1074

The space charge density on an electric field is always transferring moment to molecules by the force term $\vec{F} = e(n_p - n_e - n_n)\vec{E}$ in (25). Changes in the charge density cause changes in the transferred momentum, which cause pressure variations in the air. This are the sound waves, which can be seen in the left column of Fig. 6.

The sound waves are generated on each peak of current, and their frequency is related to the speed of the changes in the charge density and consequently to the electric current.

It can be seen on the left column of Fig. 6 that while the current is rising the pressure on a narrow region on the tip of the electrode is also rising. This pressure reaches the peak between $34.4\ \mu s$ and $34.6\ \mu s$, and after that it is possible to see this pressure front moving, the sound wave departing the tip of the electrode. As expected, the pressure of the sound wave decreases during propagation.

When the first pulse occurs, there are no previous negative ion clouds on the discharge gap. The negative ion clouds reduce the electric field near the electrode tip, so the first pulse occurs in a higher electric field. This causes the first pulse to have a higher current, and to generate a higher concentration of negative ions, which affects the next pulses. In Fig. 7 it is possible to see the first pulse, which has a significantly higher peak current, and the next 4 pulses, which have a lower current than the usual, due to the reduced electric field from the negative ion cloud produced in the first pulse.

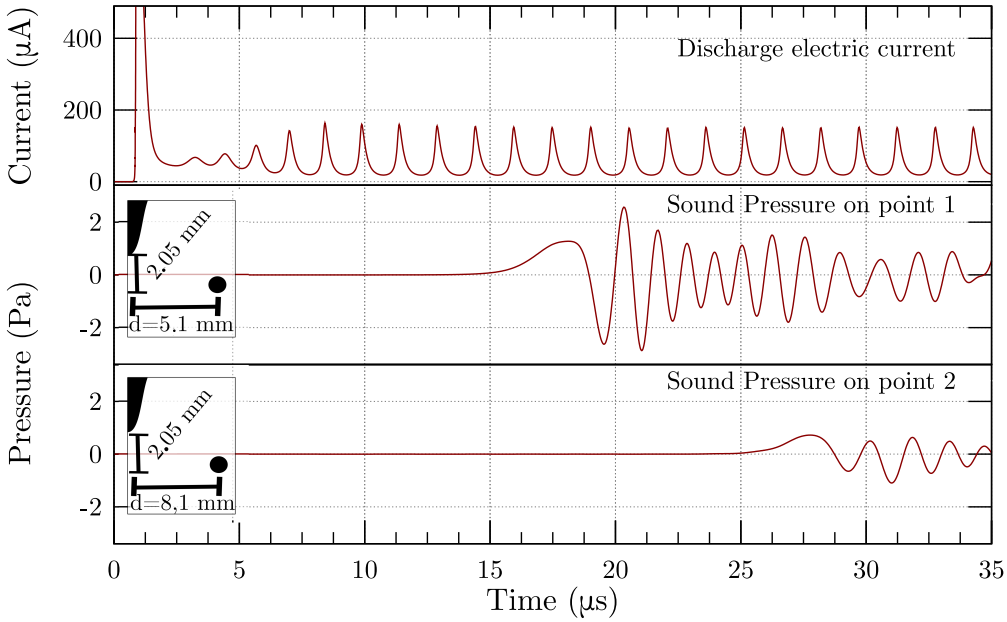

Fig. 7. Discharge current for $-6.5\ kV$, electrode-plane spacing of $6\ mm$, electrode tip curvature radius of $35\ \mu m$, and sound pressure measured on two points. The first sound pressure measurement point is located at coordinates $x = 5.1\ mm$ and $y = 3.95\ mm$ and the second at coordinates $x = 8.1\ mm$ and $y = 3.95\ mm$. The insets show the measurement point location in relation two the electrode tip.

In this figure, it is possible to note a delay between the first current pulse and the first changes in pressure on points one and two, which corresponds to the propagation time of the sound wave. Since the frequency of occurrence of the Trichel pulses during this discharge is very high, the sound waves from multiple pulses are mixed, and it is not possible to distinguish clearly the contribution of each pulse to the sound waves. It is also possible to observe the reduction of sound pressure from point one, which is closer to the electrode tip, to point two, more distant from the electrode.

In Fig. 8 the air velocity magnitude $|\vec{u}|$ is shown in the color map, and the arrows indicate the velocity direction. It is possible to notice that the discharge pulls the air from below the electrode tip, which is then pushed away in the horizontal direction and also in the top direction. The highest speed is located just below the electrode tip. This is in qualitative concordance with the experimental and simulated results from [24], which were performed in a different voltage and geometry, but are still correspondent to a negative corona discharge in the Trichel pulse regime. This reference utilized the incompressible Navier-Stokes equations to simulate the air velocity field, which cannot simulate the sound pressure as performed in this paper.

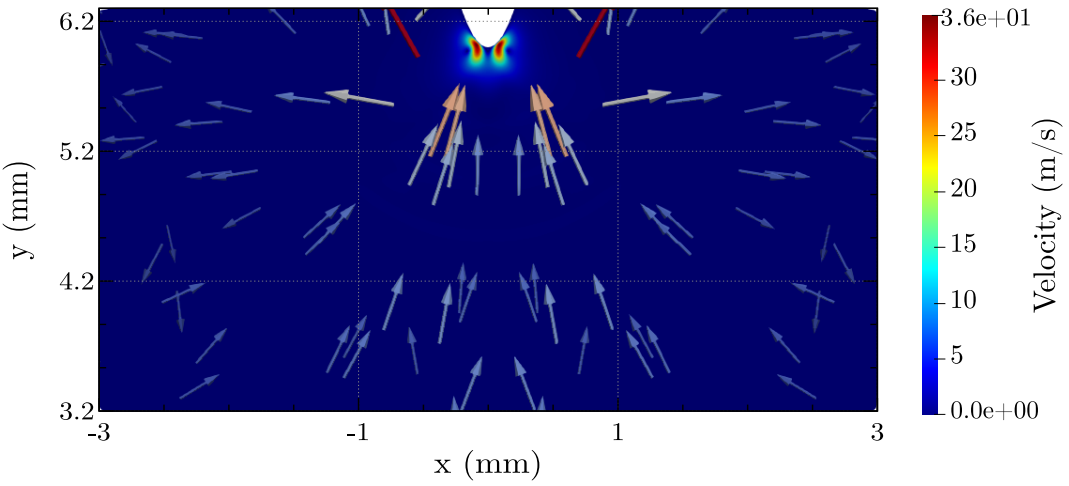

Fig. 8. Velocity field at 35 μs for the -6.5 kV discharge, electrode-plane spacing was 6 mm and electrode tip curvature radius of 35 μm. The velocity magnitude is expressed in the color map and direction in the arrows.

Fig. 9 shows the current and sound pressure when the applied voltage is lowered to -5.5 kV maintaining the geometry. The pulse peak current reduces from 154 μA to 69 μA, and the peak sound pressure on point 1 reduces from 1.7 Pa to 0.3 Pa compared to the -6.5 kV voltage. The interval between Trichel pulses increase from 1.6 μs to 3.78 μs, but the contributions of different pulses to the sound waves are still mixed.

Fig. 10 shows the current and sound pressure when the applied voltage is lowered to -5.3 kV maintaining the geometry. The sound measurement points were changed to 3 mm below the electrode for point one and 3 mm to the right of the electrode tip for point two. In this discharge, the time between Trichel pulses dropped to 8.27 μs, and it is possible now to see the sound wave produced by each individual pulse.

All the sound waves occur with a delay, measured from the current pulse, that corresponds to the propagation at the speed of sound. The sound waves can reflect on the ground plate, the instant when this reflection arrives at the measurement points one and two is indicated in this figure. After this point, the waves produced by the discharge are superimposed with the reflected waves.

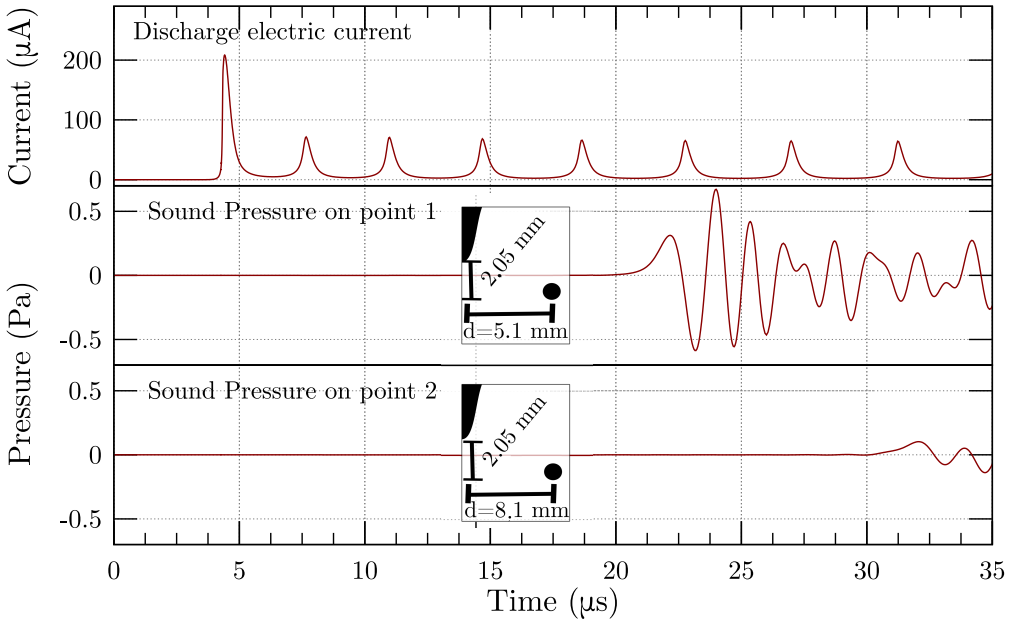

Fig. 9. Discharge current for the $-5.5\ kV$ discharge with 6 mm electrode-plane spacing and 35 μm electrode tip curvature radius and sound pressure measured on two points. The first sound pressure measurement point is located at coordinates $x = 5.1\ mm$ and $y = 3.95\ mm$ and the second at coordinates $x = 8.1\ mm$ and $y = 3.95\ mm$. The insets show the measurement point location in relation two the electrode tip.

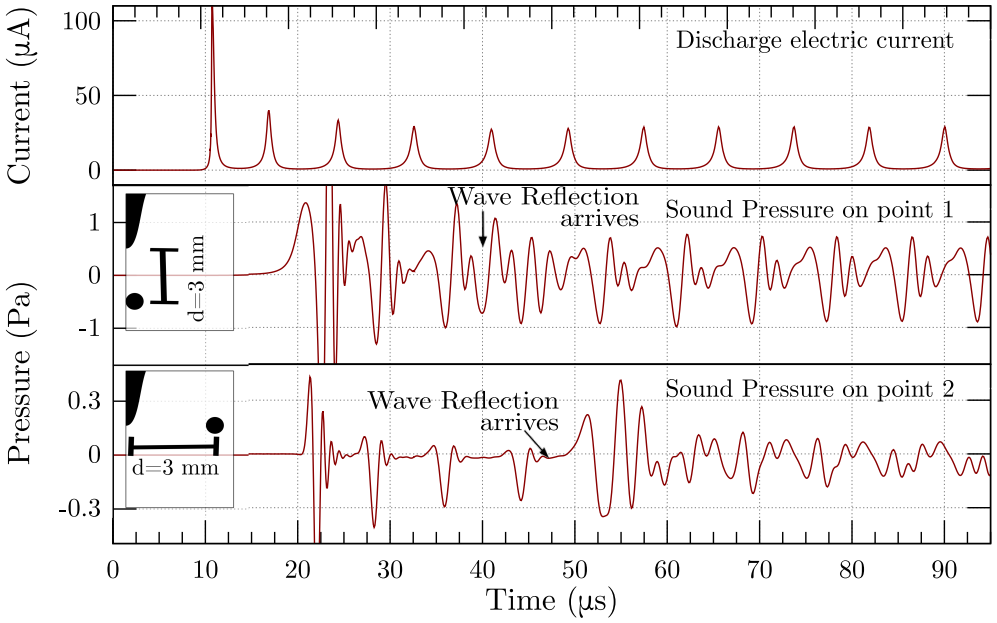

Fig. 10. Discharge current for the $-5.3\ kV$ discharge with 6 mm electrode-plane spacing and 35 μm electrode tip curvature radius and sound pressure measured on two points. The first sound pressure measurement point is located at coordinates $x = 0\ mm$ and $y = 3\ mm$ and the second at coordinates $x = 3\ mm$ and $y = 6\ mm$. The insets show the measurement point location in relation two the electrode tip.

Fig. 11 shows two pressure pulses generated by two separated Trichel pulses on the measurement point at the right of the electrode tip and below the electrode tip. Note that, despite that both of these points are located at the same distance, 3 mm from the electrode tip, there is a difference in the peak pressure of the sound wave at these two points. It is also possible to note that there are extra pulses on the point below the electrode tip, compared to the one at the side of the tip. The reason for that

ISSN 2179-1074

can be seen in Fig. 12, which shows that wave fronts 3, 4 and 5 exist both on the side and below the electrode, but wave fronts 1 and 2 exist only below the electrode.

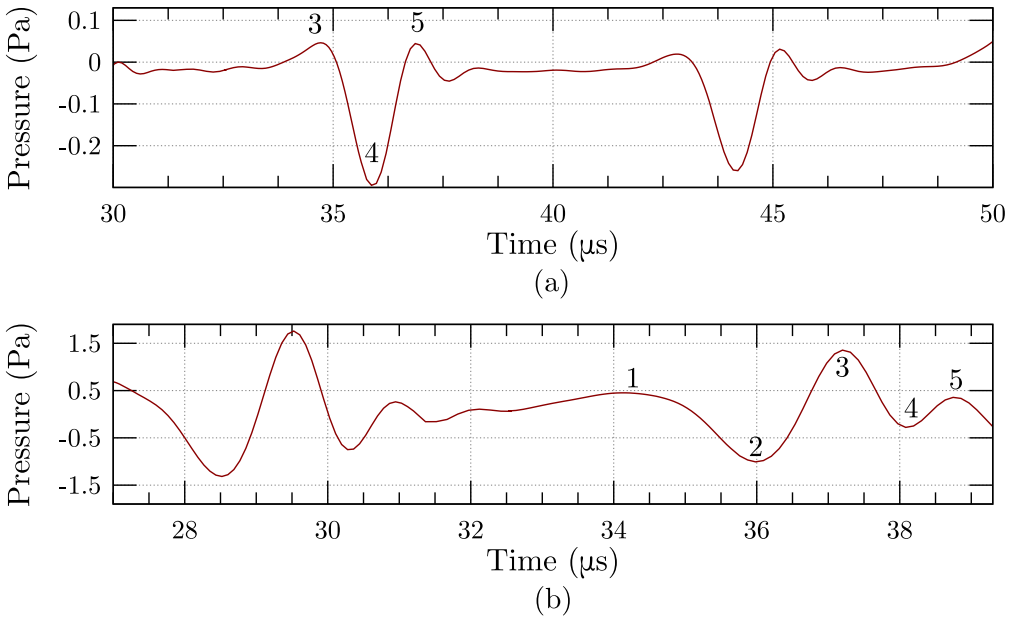

Fig. 11. Sound pressure for the $-5.3\ kV$ discharge with 6 mm electrode-plane spacing and 35 μm electrode tip curvature radius, measured at 3 mm to the right of the electrode tip (a), measured at 3 mm below the electrode tip (b).

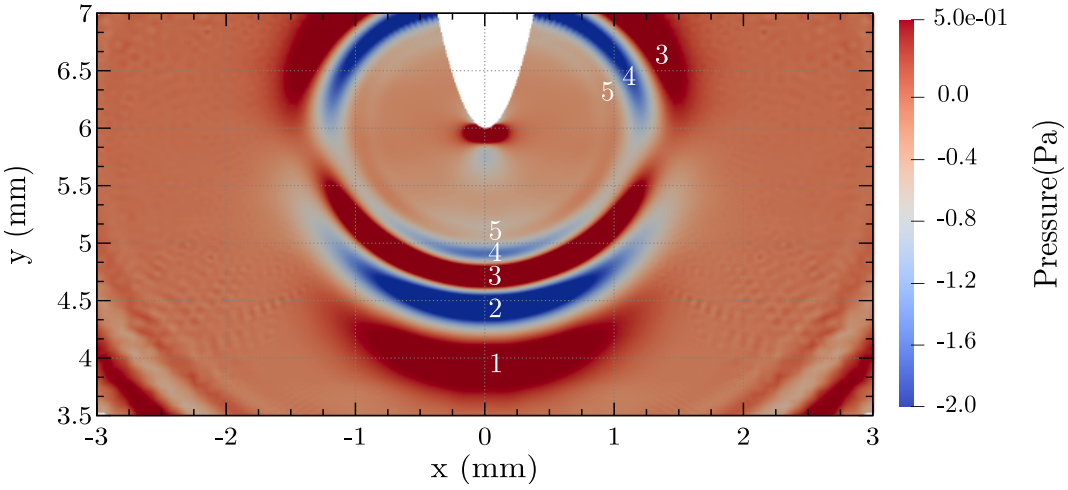

Fig. 12. Sound pressure at 29.5 μs for the $-5.3\ kV$ discharge with 6 mm electrode-plane spacing and 35 μm electrode tip curvature radius.

The pressure scale in Fig. 12 has been limited to show all the wave fronts, so there are points above and below the color scale maximum and minimum values. Notice also that on the side of the electrode tip, there is a region in which the sound wave pressure is smaller. This can explain the lower values obtained in Fig. 11 (a) compared with Fig. 11 (b), despite both points being at the same distance.

Figs. 13 to 17 show the results for the $-10\ kV$ discharge with 3 cm electrode-plane spacing and 19 μm electrode tip curvature radius. With this simulation, the electric current can be compared with experimental results from [33]. In Fig. 13 the electric field during the simulation can be seen. The highest values of the electric field are located near the electrode tip, where the ionization is larger and

the positive ions are concentrated. Free electrons are generated in this region and drift away from the electrode, generating the negative ions seen in Fig. 14, which are located below the higher electric field region.

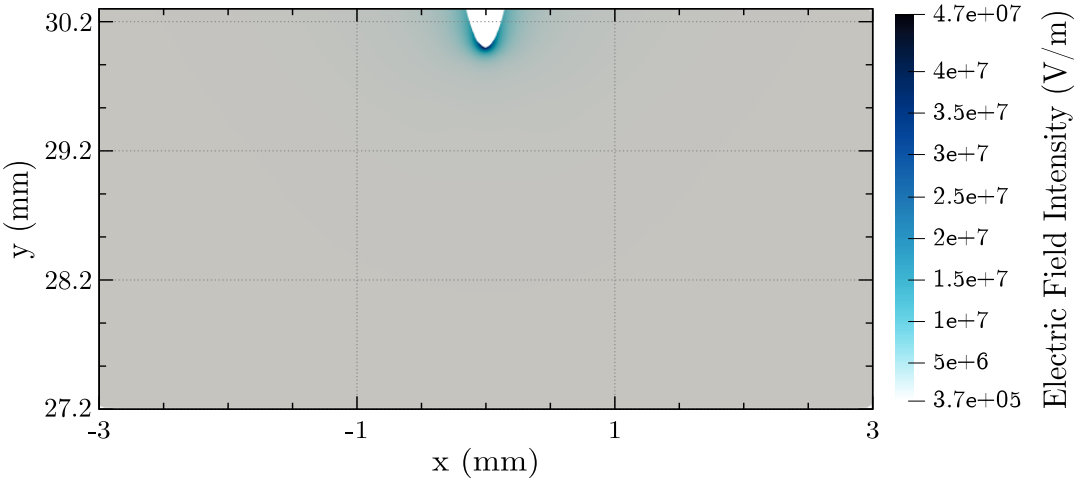

Fig. 13. Electric field intensity at 51 μs for the -10 kV discharge with 3 cm electrode-plane spacing and 19 μm electrode tip curvature radius.

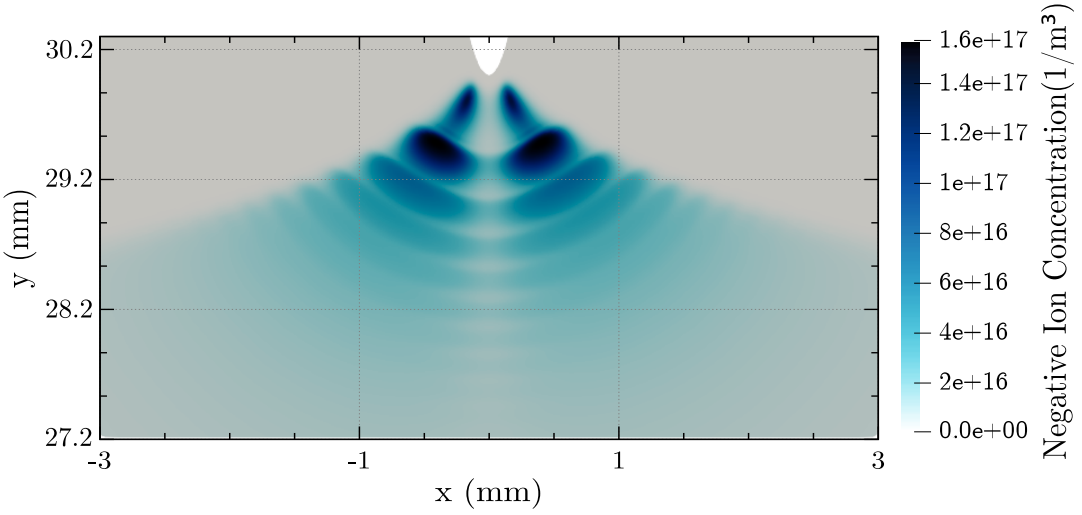

Fig. 14. Negative ion concentration at 51 μs for the -10 kV discharge with 3 cm electrode-plane spacing and 19 μm electrode tip curvature radius.

In this simulation, it is possible to notice a region with few negative ions on the symmetry axis and two clouds, one for each side. This toroidal distribution of ions during the discharge has been seen in experiments in [35]. This distribution is also observed in the electron concentration in Fig. 15. Besides this difference in relation to the previous discharges, the sound pressure format in Fig. 16 remains the same.

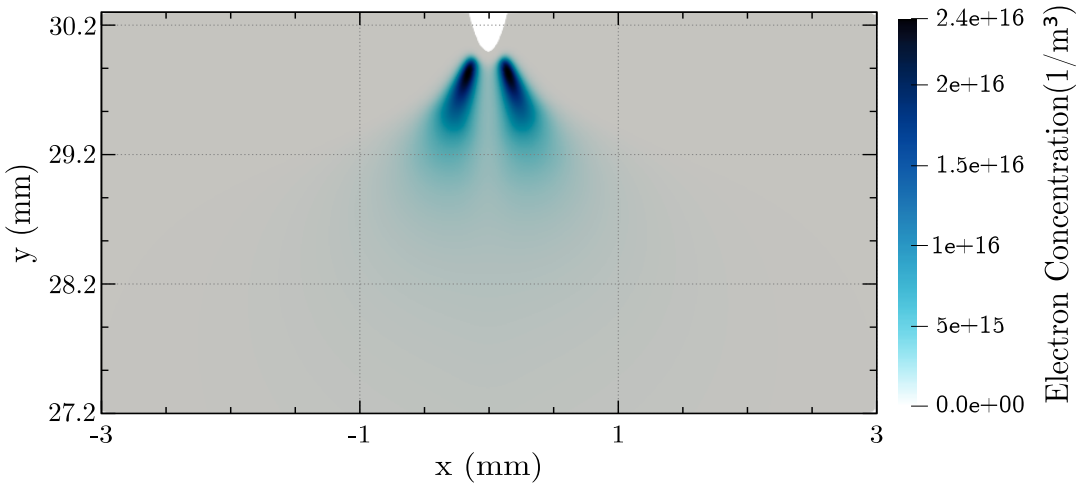

Fig. 15. Electron concentration at 51 μs for the -10 kV discharge with 3 cm electrode-plane spacing and 19 μm electrode tip curvature radius.

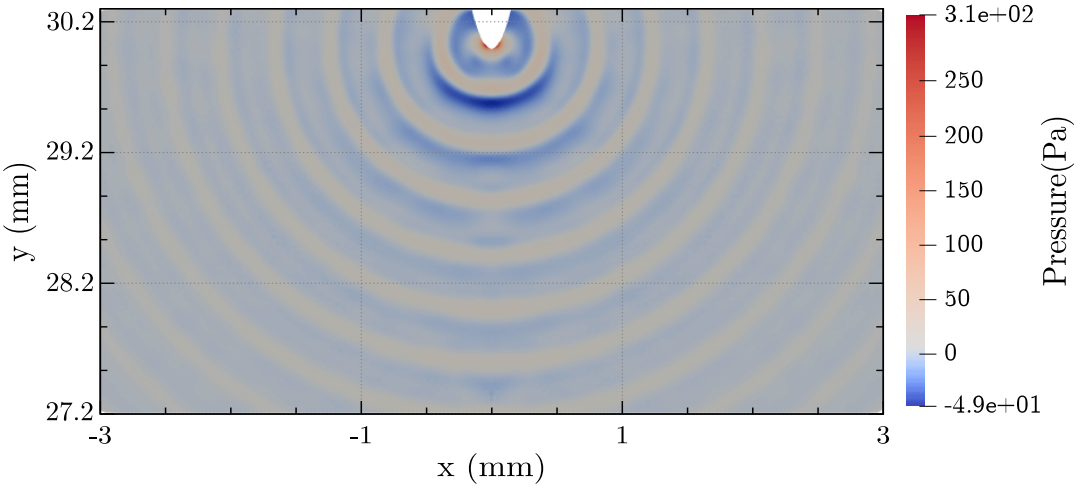

Fig. 16. Sound pressure at 51 μs for the -10 kV discharge with 3 cm electrode-plane spacing and 19 μm electrode tip curvature radius.

In Fig. 17 this discharge electric current and sound pressure on two points are shown. The inset in the current graph shows a comparison of one current pulse with experimental data from [33]. The simulated current is in good agreement with the experimental data for both pulse peak value and fall time. The only differences are the slower pulse rise, seen in the inset, and the simulation inter-pulse interval, which is 2.25 μs faster than in the experiment.

In the two sound measurement points, it is possible to notice the individual contribution of the first current pulse to the first sound wave, which has a higher amplitude. In the first point, this contribution is seen before 20 μs and in the second before 30 μs.

After these times the contributions of the different pulses are mixed, but it can be seen that slight variations that occur in the pulse current after 10 μs cause noticeable changes in the sound waves peak amplitude in the first sound measurement point.

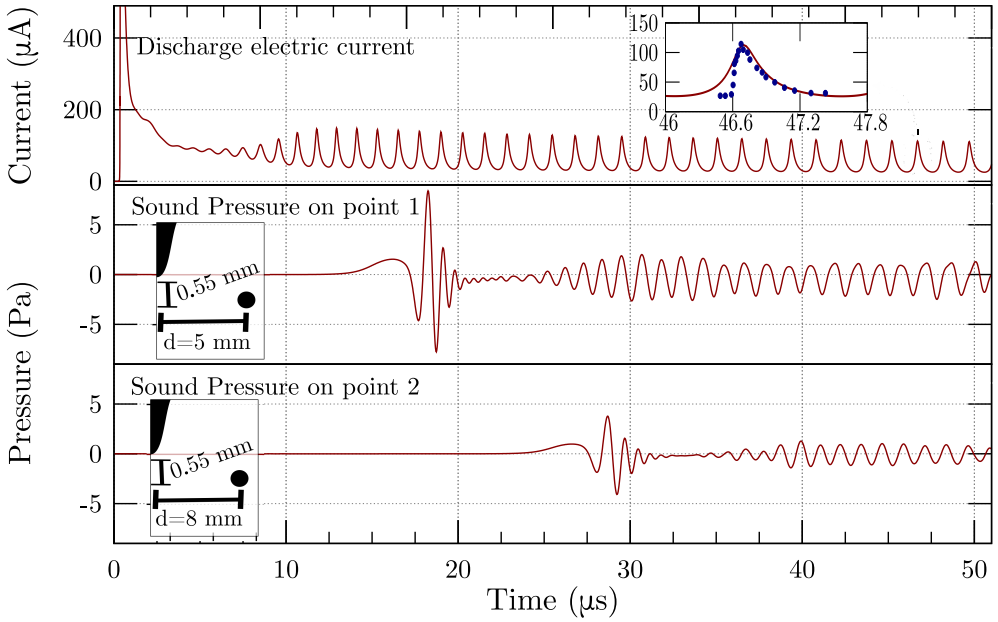

Fig. 17. Discharge current for the $-10\ kV$ discharge with 3 cm electrode-plane spacing and 19 μm electrode tip curvature radius. The first sound pressure measurement point is located at coordinates $x = 5\ mm$ and $y = 29.45\ mm$ and the second at coordinates $x = 8\ mm$ and $y = 29.45\ mm$. The insets in the sound pressure graphs show the measurement point location in relation two the electrode tip. The inset in the current graph in this figure shows the comparison between one of the current pulses of the simulation (red line) and experimental data for the same voltage and geometry (blue points), obtained from [33].

The results of the simulated electrical breakdown measured in [36] are shown below in Fig. 18 and Fig. 19. The geometry consists of an electrode tip of 150 μm radius mounted on a larger metallic piece with a curvature radius of 5 mm. The gap length is 10 mm, and the applied voltage is $+22.5\ kV$.

Fig. 18 shows the electric field and photoionization source term at various points during the propagation of the first streamer. Notice the difference between the electric field in this figure, which corresponds to a streamer, to the electric field in Fig. 13, which corresponds to the electric field of a corona discharge in the Trichel pulse regime.

The electric field of Fig. 13 has higher values always located near the electrode tip since the charge density is not high enough to distort the field generated by the applied voltage, and as a consequence the ionization region of the discharge is also located at the electrode tip. In the streamer, the charge density is much higher, and the electric field is distorted. This causes the ionization region to propagate along the streamer gap, in this case until it reaches the ground plate.

The positive streamer propagates because of electrons generated in front of the streamer tip by ionization from photons produced in the discharge, the S_{ph} term shown in Fig. 18. These electrons are attracted in the direction of the streamer tip, ionizing other atoms due to collisions. Notice also that the field inside the streamer is screened due to the accumulation of space charge on the borders of the discharge.

The first streamer propagation phase, which corresponds to the plateau in the current between 2 ns and 11 ns in Fig. 19, reaches the ground electrode. After the arrival, a second streamer is initiated, which, because of the already present charges left in the gap from the first streamer, is stronger than the first one. This corresponds to the current rise after 11 ns. After the second streamer peak finishes, the current keeps flowing, causing an increase in the temperature and expansion of the heated gas, along

with the accumulation of ions. This causes the increase of the ionization coefficient, leading to the breakdown of the discharge gap, when the thermionic effect starts to be significant and the transition to electric arc occurs [37].

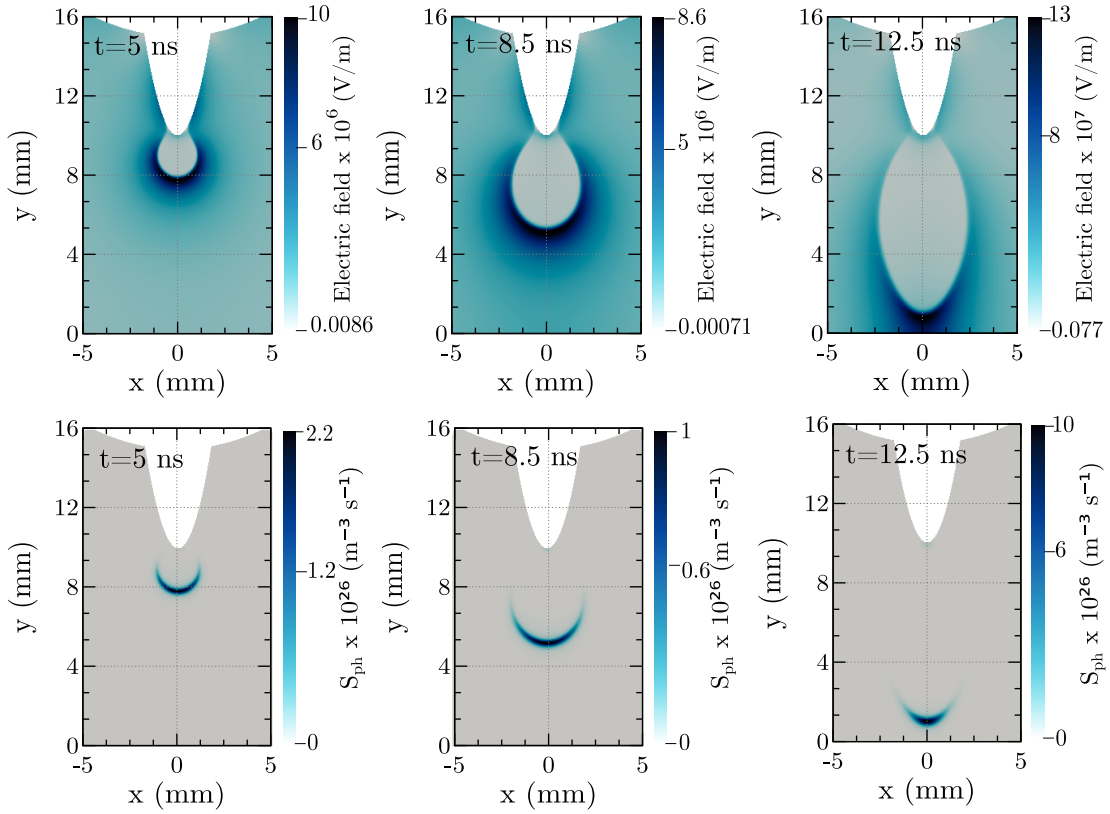

Fig. 18. Electric field and photoionization source term S_{ph} in a simulation with an electrode tip with 150 μm radius mounted on a larger metallic piece with a curvature radius of 5 mm. The gap length is 10 mm and the applied voltage is $+22.5$ kV.

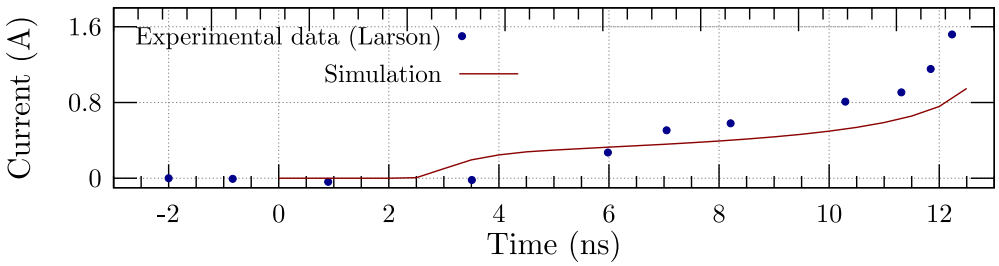

Fig. 19. Simulated electric current for a discharge with an electrode tip with 150 μm radius mounted on a larger metallic piece with a curvature radius of 5 mm. The gap length is 10 mm and the applied voltage is $+22.5$ kV. The simulated curve (red line) is superimposed with the experimental data (blue points) for the same voltage and geometry obtained from [36].

Fig. 20 shows the simulated sound pressure and electric field for $+14$ kV streamer discharge with 25 mm gap length and 100 μm electrode tip curvature radius. Experimental data for this discharge is available at [38]. In this figure, one sound wave can be seen departing from the electrode tip and another one from the whole streamer length. There are also sound waves produced when the streamer arrives at the ground electrode. This is different from the previous simulations of the corona discharge on the Trichel pulse regime, where only the sound wave departing from the electrode tip is produced. This is due to the difference in charge concentration and electric field distribution during the discharges.

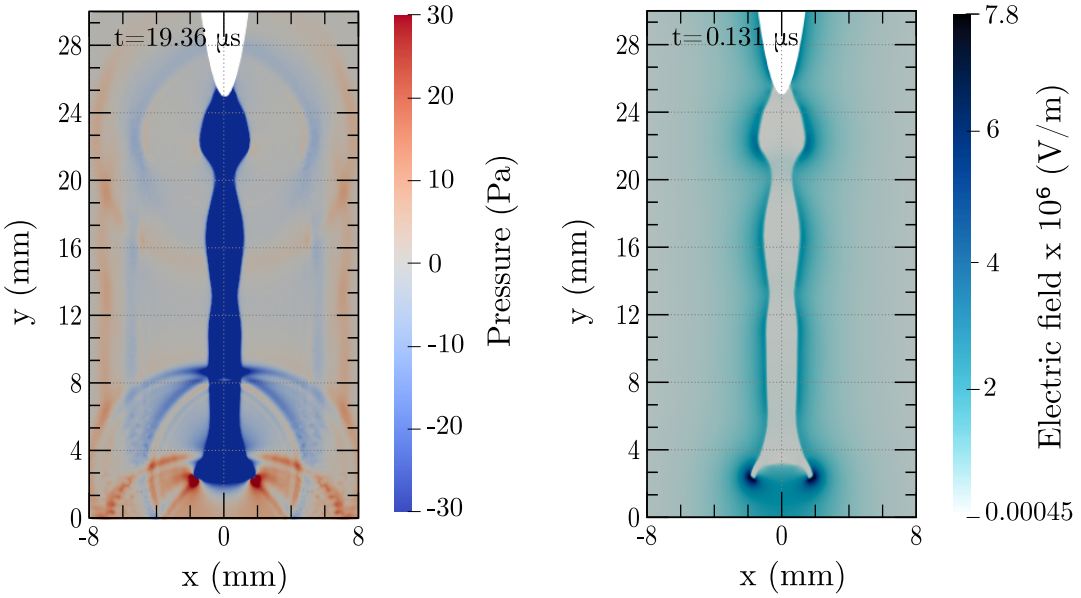

Fig. 20. Simulated sound pressure and electric field for $+14\ kV$ streamer discharge with 25 mm gap length and 100 um electrode tip curvature radius.

During the Trichel pulses in the previous simulation, the electric field and charge maximum concentration values are concentrated in a narrow region close to the electrode tip, so this is the region where there is more momentum transfer between ions and electrons and molecules, and consequently, the sound waves are generated in this region. In this simulation, the electric field highest value, as well as the charge concentration maximum, occur at the streamer tip. Due to the fast propagation of the streamer, the wave appears as generated from the whole discharge length. Both sound waves generated during the streamer, the one that depart from the electrode tip and the one that originates from the whole extension of the discharge have been observed experimentally in the literature using Schlieren photography [39], [40]. The existence of the momentum transfer in the whole length of the discharge gap for the streamer and only at the electrode tip for the Trichel pulses is also supported by experimental measurements of generated ionic wind in [38].

Fig. 21 shows the comparison between the simulated current for the $-30\ kV$ discharge with 6 cm electrode-plane spacing and 0.3 mm electrode tip curvature radius. Experimental data for the same geometry and $-40\ kV$ [41] is superimposed in blue.

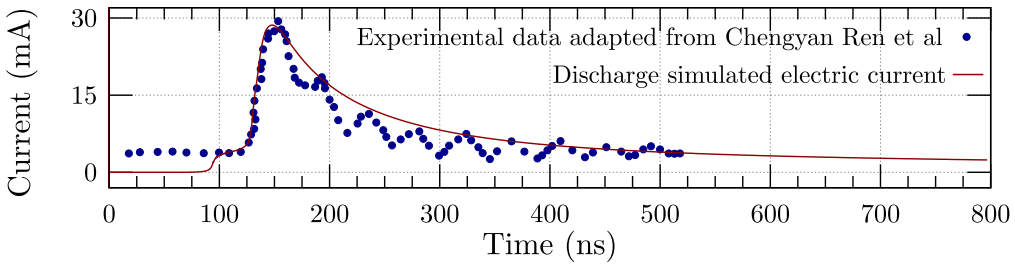

Fig. 21. Discharge current for the $-30\ kV$ discharge with 6 cm electrode-plane spacing and 0.3 mm electrode tip curvature radius. Experimental data for the same geometry [41] is superimposed in blue.

Since the separation between the current pulses in this discharge is big (approximately 2 ms), only the

ISSN 2179-1074

first pulse was seen in the simulation since simulating for this time would take too much computational time. Notice that, as observed in the previous discharges, the first Trichel pulse has a larger current than the next pulses. This can explain the concordance in peak current between the two different voltages in the same geometry. The lower voltage for the simulation was chosen in order to make a comparison between the simulated sound wave to the experimental one for a current pulse with the same amplitude.

The red line in Fig. 22 shows the sound pressure produced by the $-30\ kV$ discharge with $6\ cm$ electrode-plane spacing and $0.3\ mm$ electrode tip curvature radius measured on the side of the electrode at $20\ cm$ distance. Experimental data for the sound pressure in the same geometry is available in [41], also measured at approximately at $20\ cm$ from the electrode. This data is superimposed to simulation results in fig. 22 as the blue points.

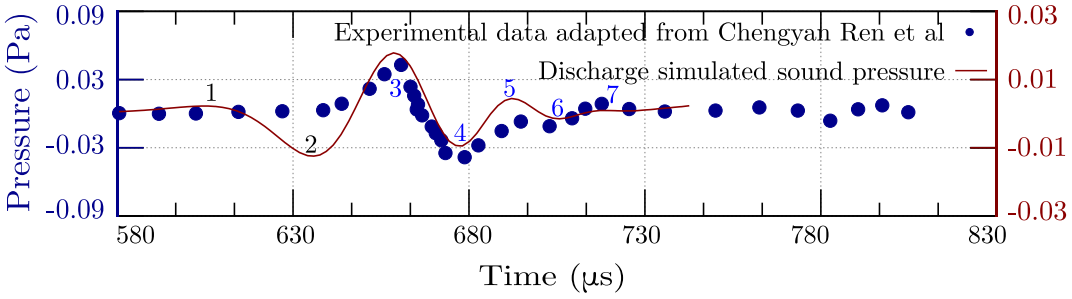

Fig. 22. Sound pressure was produced by the $-30\ kV$ discharge with $6\ cm$ electrode-plane spacing and $0.3\ mm$ electrode tip curvature radius measured on the side of the electrode at $20\ cm$ distance. Experimental data for the sound pressure in the same geometry exists in [41] measured at $20\ cm$ from the electrode.

The curve format shows good agreement with the experimental results, with peaks and valleys 3 to 7 coinciding. The first Trichel pulse produces two additional wave fronts which are not present in sound waves for the next pulses, this can be verified by comparing the first and second pulse on sound measurement point 2 in Fig. 10, for the $-5.3\ kV$ simulation. Since for this simulation only the first pulse was observed, this can explain the presence of points 1 and 2 in the waveform on Fig. 22, which are not present on the experimental results. Since the sound waves have a high frequency and high pressure near the electrode tip, as they propagate they are subjected to nonlinear and thermoviscous effects that cause pulse widening [42]–[44].

Fig. 23 shows a comparison between average pulse current and peak sound pressure at $5.5\ mm$ to the side of the electrode tip for all simulated discharges in the Trichel pulses regime. The graph shows that there is a relationship between average pulse current and sound pressure independent of the simulation geometry for the performed simulations.

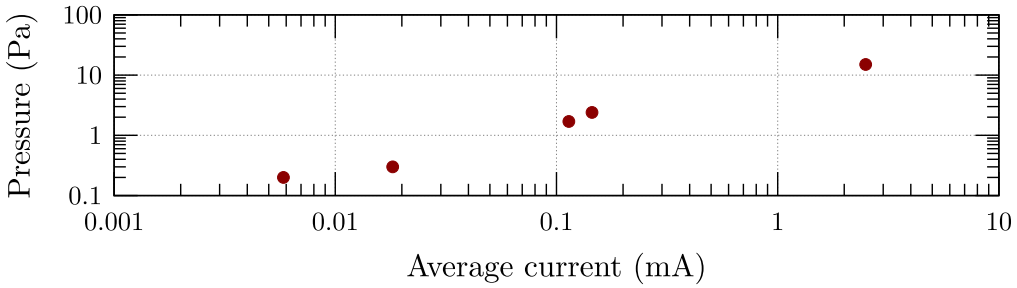

Fig. 23. Comparison between average pulse current and peak sound pressure at $5.5\ mm$ to the side of the electrode tip for all simulated discharges in the Trichel pulses regime.

ISSN 2179-1074

V. CONCLUSION

As partial discharges can occur in different types of electric equipment, causing progressive deterioration of the insulation, there is great interest in developing techniques to detect partial discharges, such as those based on the detection of ultrasonic emission. However, as various effects can co-occur during a discharge, it is difficult to identify characteristics in sound waveforms and correlate them with discharge characteristics. In this sense, the approach used in this work and the results obtained can assist in the efforts to measure partial discharges effects and correlate them with the discharge characteristics.

The approach used in this work was efficient in simulating ultrasonic waves produced by partial discharges, as the obtained results agree with experimental results reported in the literature. The simulations, which were based on the coupling between the three-species drift-diffusion model considering photoionization, and the linearized compressible Navier-Stokes equations, successfully produced ultrasonic waves. In the previous literature only the coupling with incompressible laminar flow Navier-Stokes equations have been simulated, so those works could only simulate ionic wind produced by the Trichel pulses, but no sound. In this work, both streamers and Trichel pulses were simulated for the needle-plane geometry in the air with the same set of parameters, whereas previously reported works have focused either on streamers or Trichel pulses. The sound waves produced by both types of partial discharges were successfully simulated.

The simulations demonstrated that the sound waves depart from the electrode tip for the Trichel pulses, whereas for the streamers two sound waves are produced, one from the electrode tip and the other from the whole discharge length. This is also in accordance with experimental results from the literature.

Differences in the wavefront with respect to its relative position to the electrode tip were observed, with analysis conducted for the variations in the sound wave format depending on the measurement position relative to the electrode tip for the Trichel pulses. These results have shown that the sound wave is not spherical near the discharge spot.

The sound wave for one of the discharges in the Trichel pulse regime was compared with experimental results in the literature, and results are in good agreement for the wave format.

The electric current and charge per pulse were compared with experimental results reported in the literature for the same discharge conditions. The simulation results for the electric current have good concordance with the literature for rise time, fall time and peak value for the simulations performed for both Trichel pulses and streamers.

The model could also predict the formation of streamers or Trichel pulses correctly for the situations tested with the same set of parameters, when normally, in the literature only one discharge type is simulated.

Discharge characteristics in the electric field and charged species distributions were observed in the simulations, including the toroidal distribution of ions observed in experiments in the literature.

Both current and sound waves were correlated with the discharge characteristics, results that can be used to help in the detection of partial discharges.

Future simulations are in progress to access the effects of the simulated sound waves on an optical fiber, so that the utilization of Fiber Bragg Gratings to detect partial discharges by analyzing ultrasonic waves can be studied. The research group is presently performing experiments with this objective.

Brazilian Microwave and Optoelectronics Society-SBMO *received 02 May 2022; for review 12 May 2022; accepted 25 Sept 2022*
Brazilian Society of Electromagnetism-SBMag *ISSN 2179-1074*

ACKNOWLEDGMENTS

The authors acknowledge CAPES (Coordination of Superior Level Staff Improvement), CNPQ (National Council for Scientific and Technological Development), FINEP (Funding Authority for Studies and Projects), Araucária Foundation, and SETI (State Secretary of Science, Technology, and Higher Education of Paraná), and Multi-User Photonics Facility - UTFPR-CT. This study was financed in part by the Coordenação de Aperfeiçoamento de Pessoal de Nível Superior - Brasil (CAPES) - Finance Code 001.

REFERENCES

[1] N. Lutz, "A generalized approach to partial discharge modeling," *IEEE Transactions on Dielectrics and Electrical Insulation*, vol. 2, no. 4, pp. 510–528, Aug. 1995.

[2] R. Sousa Ferreira, "Estudo De Descargas Parciais Em Isolamento De Máquinas Elétricas Usando O Método Dos Elementos Finitos," Ph.D. dissertation, UFRJ/COPPE, Rio de Janeiro, Feb. 2017.

[3] S. Boggs, "Partial discharge. III. Cavity-induced PD in solid dielectrics," *IEEE Electrical Insulation Magazine*, vol. 6, no. 6, pp. 11–16, Nov. 1990.

[4] A. Gjerde, "Multifactor ageing models - origin and similarities," *IEEE Electrical Insulation Magazine*, vol. 13, no. 1, pp. 6–13, Jan. 1997.

[5] J. H. Mason, "Enhancing the significance of pd measurements," *IEEE Transactions on Dielectrics and Electrical Insulation*, vol. 2, no. 5, pp. 876–888, 1995.

[6] Conseil international des grands réseaux électriques and Comité d'études D1, *Guide for partial discharge measurements in compliance to IEC 60270*. Paris: CIGRÉ, 2008.

[7] G. Callender, "Modelling partial discharge in gaseous voids," Ph.D. dissertation, University of Southampton, Mar. 2018.

[8] A. Nasr Esfahani, S. Shahabi, and B. Kordi, "Partial discharge detection and identification at low air pressure in noisy environment," *High Voltage*, vol. 6, no. 5, pp. 850–860, Oct. 2021.

[9] Y. Wang, X. Li, Y. Gao, H. Zhang, D. Wang, and B. Jin, "Partial Discharge Ultrasound Detection Using the Sagnac Interferometer System," *Sensors*, vol. 18, no. 5, p. 1425, May 2018.

[10] R. Schwarz, T. Judendorfer, and M. Muhr, "Review of partial discharge monitoring techniques used in high voltage equipment," in *2008 Annual Report Conference on Electrical Insulation and Dielectric Phenomena*, pp. 400–403, 2008.

[11] W. M. Huamán Cuenca, "Caracterização dos Sinais de Descargas Parciais em Equipamentos de Alta Tensão a Partir de Modelos Experimentais," Ph.D. dissertation, Universidade Federal do Rio de Janeiro, COPPE, 2005.

[12] C. Shi, G. Ma, N. Mao, Q. Zhang, Q. Zheng, C. Li, and S. Zhao, "Ultrasonic detection coherence of fiber Bragg grating for partial discharge in transformers," in *2017 IEEE 19th International Conference on Dielectric Liquids (ICDL)*, pp. 1–4, June 2017.

[13] X. Wang, B. Li, H. Roman, O. Russo, K. Chin, and K. Farmer, "Acousto-optical PD Detection for Transformers," *IEEE Transactions on Power Delivery*, vol. 21, no. 3, pp. 1068–1073, July 2006.

[14] I. B. V. da Costa, G. H. Weber, D. F. Gomes, J. R. Galvão, M. J. da Silva, D. R. Pipa, A. Ozcáriz, C. R. Zamarreño, C. Martelli, and J. C. Cardozo da Silva, "Electric discharge detection and localization using a distributed optical fiber vibration sensor," *Optical Fiber Technology*, vol. 58, p. 102266, Sept. 2020.

[15] C. Forssén, "Modelling of cavity partial discharges at variable applied frequency," Ph.D. dissertation, Electromagnetic Engineering, Elektroteknisk teori & konstruktion, Stockholm, 2008.

[16] L. Liu, "Physics of Electrical Discharge Transitions in Air," Ph.D. dissertation, KTH Royal Institute of Technology, Stockholm, Sweden, 2017.

[17] P. Dordizadeh, K. Adamiak, and G. S. Peter Castle, "Numerical investigation of the formation of Trichel pulses in a needle-plane geometry," *Journal of Physics D: Applied Physics*, vol. 48, no. 41, Oct. 2015.

[18] P. Dordizadeh, K. Adamiak, and G. S. Peter Castle, "Study of the impact of photoionization on negative and positive needle-plane corona discharge in atmospheric air," *Plasma Sources Science and Technology*, vol. 25, no. 6, Oct. 2016.

[19] J. Karel, "Numerical simulation of streamer propagation on unstructured dynamically adapted grids," Ph.D. dissertation, Université Paris-Nord - Paris XIII, Dec. 2014.

[20] Y. V. Serdyuk and S. M. Gubanski, "Computer modeling of interaction of gas discharge plasma with solid dielectric barriers," *IEEE Transactions on Dielectrics and Electrical Insulation*, vol. 12, no. 4, pp. 725–735, Aug. 2005.

received 02 May 2022; for review 12 May 2022; accepted 25 Sept 2022

ISSN 2179-1074

[21] J. Zhang, K. Adamiak, and G. Castle, "Numerical modeling of negative-corona discharge in oxygen under different pressures," *Journal of Electrostatics*, vol. 65, no. 3, pp. 174–181, Mar. 2007.

[22] P. Sattari, G. S. P. Castle, and K. Adamiak, "Numerical Simulation of Trichel Pulses in a Negative Corona Discharge in Air," *IEEE Transactions on Industry Applications*, vol. 47, no. 4, pp. 1935–1943, July 2011.

[23] L. Papageorgiou, A. C. Metaxas, and G. E. Georghiou, "Three-dimensional numerical modelling of gas discharges at atmospheric pressure incorporating photoionization phenomena," *Journal of Physics D: Applied Physics*, vol. 44, no. 4, Feb. 2011.

[24] S. Chen, J. C. P. Y. Nobelen, and S. Nijdam, "A self-consistent model of ionic wind generation by negative corona discharges in air with experimental validation," *Plasma Sources Science and Technology*, vol. 26, no. 9, Aug. 2017.

[25] G. E. Georghiou, A. P. Papadakis, R. Morrow, and A. C. Metaxas, "Numerical modelling of atmospheric pressure gas discharges leading to plasma production," *Journal of Physics D: Applied Physics*, vol. 38, no. 20, Oct. 2005.

[26] C. Pan, Y. Meng, K. Wu, Z. Han, K. Qin, and Y. Cheng, "Simulation of partial discharge sequences using fluid equations," *Journal of Physics D: Applied Physics*, vol. 44, no. 25, June 2011.

[27] A. A. Kulikovsky, "Positive streamer between parallel plate electrodes in atmospheric pressure air," *Journal of Physics D: Applied Physics*, vol. 30, no. 3, pp. 441–450, Feb. 1997.

[28] J. Wang, R. Guo, A. Ping, T. Liu, S. Han, and Q. Li, "Research on numerical simulation for partial discharge of epoxy interface excited by high-frequency sinusoidal voltage," *High Voltage*, vol. 7, no. 3, pp. 439–451, June 2022.

[29] M. B. Zhelezniak, A. K. Mnatsakanian, and S. V. Sizykh, "Photoionization of nitrogen and oxygen mixtures by radiation from a gas discharge," *Teplofizika vysokikh temperatur*, vol. 20, no. 3, pp. 423–428, 1982.

[30] L. Liu and M. Becerra, "An efficient model to simulate stable glow corona discharges and their transition into streamers," *Journal of Physics D: Applied Physics*, vol. 50, no. 10, Mar. 2017.

[31] S. Nijdam, J. Teunissen, and U. Ebert, "The physics of streamer discharge phenomena," *Plasma Sources Science and Technology*, vol. 29, no. 10, Nov. 2020.

[32] N. Sato, "Discharge current induced by the motion of charged particles," *Journal of Physics D: Applied Physics*, vol. 13, no. 1, pp. L3–L6, Jan. 1980.

[33] P. Dordizadeh Basirabad, "Numerical and Experimental Study of the Trichel Pulses in Needle-plane Geometry," Ph.D. dissertation, Sept. 2016.

[34] W. L. Lama and C. F. Gallo, "Systematic study of the electrical characteristics of the "Trichel" current pulses from negative needle-to-plane coronas," *Journal of Applied Physics*, vol. 45, no. 1, Jan. 1974.

[35] A. Sun, X. Zhang, Y. Guo, Y. He, and G. Zhang, "Review on ionization and quenching mechanisms of Trichel pulse*," *Chinese Physics B*, vol. 30, no. 5, May 2021.

[36] A. Larsson, "The effect of a large series resistance on the streamer-to-spark transition in dry air," *Journal of Physics D: Applied Physics*, vol. 31, no. 9, pp. 1100–1108, May 1998.

[37] G. V. Naidis, "Dynamics of streamer breakdown of short non-uniform air gaps," *Journal of Physics D: Applied Physics*, vol. 38, no. 21, pp. 3889–3893, Nov. 2005.

[38] E. Moreau, P. Audier, and N. Benard, "Ionic wind produced by positive and negative corona discharges in air," *Journal of Electrostatics*, vol. 93, pp. 85–96, June 2018.

[39] R. Ono and T. Oda, "Visualization of Streamer Channels and Shock Waves Generated by Positive Pulsed Corona Discharge Using Laser Schlieren Method," *Japanese Journal of Applied Physics*, vol. 43, no. 1, pp. 321–327, Jan. 2004.

[40] A. Lo, A. Cessou, C. Lacour, B. Lecordier, P. Boubert, D. A. Xu, C. O. Laux, and P. Vervisch, "Streamer-to-spark transition initiated by a nanosecond overvoltage pulsed discharge in air," *Plasma Sources Science and Technology*, vol. 26, no. 4, p. 045012, Mar. 2017.

[41] C. Ren, J. Wang, P. Yan, T. Shao, C. Zhang, and S. Zhang, "Experimental Study on Sound Characteristics Produced by DC Corona and Pulsed Discharges," *IEEE Transactions on Plasma Science*, vol. 44, no. 10, pp. 2196–2203, Oct. 2016.

[42] M. M. Karzova, P. V. Yuldashev, V. A. Khokhlova, S. Ollivier, E. Salze, and P. Blanc-Benon, "Characterization of spark-generated *N*-waves in air using an optical schlieren method," *The Journal of the Acoustical Society of America*, vol. 137, no. 6, pp. 3244–3252, June 2015.

[43] W. M. Wright, "Propagation in air of *N* waves produced by sparks," *The Journal of the Acoustical Society of America*, vol. 73, no. 6, pp. 1948–1955, June 1983.

[44] P. Yuldashev, S. Ollivier, M. Averiyanov, O. Sapozhnikov, V. Khokhlova, and P. Blanc-Benon, "Nonlinear propagation of spark-generated *N*-waves in air: Modeling and measurements using acoustical and optical methods," *The Journal of the Acoustical Society of America*, vol. 128, no. 6, pp. 3321–3333, Dec. 2010.

received 02 May 2022; for review 12 May 2022; accepted 25 Sept 2022

ISSN 2179-1074